

Contour current driven continental slope-situated sandwaves with effects from secondary current processes on the Barents Sea margin offshore Norway



Edward L. King^a, Reidulv Bøe^b, Valérie K. Bellec^b, Leif Rise^b, Jofrid Skarðhamar^c, Bénédicte Ferré^d, Margaret F.J. Dolan^b

^a Geological Survey of Canada-Atlantic (GSC-A), 1 Challenger Drive, P.O. Box 1006, Dartmouth, Nova Scotia B2Y 4A2, Canada

^b Geological Survey of Norway (NGU), P.O. Box 6315 Sluppen, N-7491 Trondheim, Norway

^c Institute of Marine Research (IMR), P.O. Box 6404, N-9294 Tromsø, Norway

^d CAGE—Centre for Arctic Gas Hydrate, Environment and Climate, Department of Geology, University of Tromsø (UiT), NO-9037 Tromsø, Norway

ARTICLE INFO

Article history:

Received 27 March 2013

Received in revised form 3 April 2014

Accepted 6 April 2014

Available online 15 April 2014

Communicated by J.T. Wells

Keywords:

sandwave morphometrics
subaqueous dune
sand transport
Norwegian Atlantic Current
contour current
deep Ekman effect
internal wave
glacigenic debris flow

ABSTRACT

Seabed data acquired from the southern Barents Sea continental margin offshore Norway reveal detailed morphology of large sandwave fields. Multibeam echosounder bathymetry and backscatter, shallow seismic, sediment samples and seabed video data collected by the MAREANO program have been used to describe and interpret the morphology, distribution and transport of the sandwaves. The bedforms lie on a slope dominated by relict glacial forms and muddy/sandy/gravelly sediments. Sandwave migration across small gravity mass failures of the glacial mud constrains the field initiation as early post glacial or later. The contour-parallel nature of the fields and crests normal to the bathymetry contours and the geostrophic Norwegian Atlantic Current (NwAC) demonstrate that the NNW-flowing oceanographic circulation is the primary driving current. The fields coincide with the depth range at which a transition between warm, saline and underlying cooler, less saline waters fluctuate across the seabed. Statistically rigorous measurements of height, width and various parameters of slope and symmetry confirm a tendency to downstream (NNW) sandwave migration but with significant exceptions. Anomalous bedform symmetry domains within the fields are tuned to meso-scale topography along (relict) glacial debris flow chutes, indicating current focusing. Upstream and upper slope-derived winnowed sand transport eroded from the glacial sediments is the supposed source. Sandwave flank slope values are comparable to the regional slope such that the gravitational vector would have a cumulative downslope migration affect unless balanced by upslope drivers. Perpendicular cross-cutting of stoss face 3-D ripples by linear (2-D) ripples in the sandwave troughs and lee faces is evidence for non-synchronous, episodic current variations. Though deep Ekman transport and internal wave action are unproven here, these could explain chute-related tuning of bedform symmetry through funneling in the debris flow chutes and favor sand recycling, thus contributing to long-term maintenance of the sandwave field.

Crown Copyright © 2014 Published by Elsevier B.V. All rights reserved.

1. Introduction

The focus of this study is recently surveyed upper-slope situated sandwave fields in the SW Barents Sea of the Norwegian continental margin. Sandwaves are indicative of strong currents that potentially challenge water column and seabed engineering operations. Their dynamic nature poses challenges for seabed infrastructure such as pipelines and cables. While shelf-situated sandwaves are well documented on a global scale, the nearest located on the adjacent shelf (Bøe et al., 2009), known occurrences of present-day slope-situated sandwaves under a contour current influence are limited. These include examples

on the Canary Islands (Wynn et al., 2000), the South China Sea (Damuth, 1980; Reeder et al., 2011), the Strait of Gibraltar (Heezen and Hollister, 1971), Gulf of Cadiz (Kenyon and Belderson, 1973; Baraza et al., 1999; Habgood et al., 2003; Mulder, 2003; Hanquiez et al., 2007), and the Faeroe–Shetland Channel (Masson, 2001). Sandwaves in this study were first noted from sidescan investigations by Kenyon (1986) who attributed them to poleward current and suggested the potential of sand transport to the deep sea through associated channels.

Factors controlling deposition of continental shelf bottom-current sands (by tidal, wave and geostrophic currents) include hydrodynamic regime (seconds to years time scale), availability of sandy sediments (accumulation, export and preservation potential) and physiographic context of the area swept by the currents (Viana et al., 1998a, 1998b).

E-mail addresses: eking@nrcan.gc.ca (E.L. King), Reidulv.Boe@ngu.no (R. Bøe), jofrid.skardhamar@imr.no (J. Skarðhamar), bfe000@post.uit.no (B. Ferré).

All are modulated by a long-term (post-glacial) global sea-level and climate regime. The slope-setting processes affecting sandwaves are more poorly understood; those driven by contour currents are not well represented in the literature. A summary of deep-water sediment wave forms by Wynn and Stow (2002) shows dominance of those classified as “bottom current waves” and “turbidity current waves”. The former are generally associated with contouritic drifts, are generally larger, aligned oblique to the contours, muddy, bioturbated, and have long-term growth and transport histories. The latter are normally associated with turbidite channels and levees, often with crestlines parallel to contours, wavelengths changing downslope, and comprising a mix of turbidites and hemipelagic sediments. The Barents Sea sandwave fields contrast in a uniformly sand composition, constant contour-normal crestline orientation, relative independence of slope topographic perturbations and relatively short-lived (post-glacial) history.

Following the terminology of Belderson et al. (1982) we use the term sandwave to refer to the subaqueous, lower flow regime, transverse bedforms of sand that have wavelengths larger than sand ripples. Where two or more sizes of sandwaves occur together or superimposed it is convenient to refer to them as small sandwaves (identical to dunes or megaripples; see discussions in Allen, 1980; Amos and King, 1984; Ashley, 1990) and large sandwaves, without implying any genetic difference in the terminology. This is because there appears to be a complete gradation in size, plan view and lee slope angle between sandwaves at various locations (Belderson et al., 1982). In our study area the driving current is generally from SSE to NNW, along the Tromsøflaket slope, and the southern bedform face is referred to as stoss and the northern as lee except where noted.

The ultimate aim of the ongoing sandwave study is to elucidate governors of process, sand source, age of the bedform field and present mobility. Initial results of the sandwave study are reported in King et al. (2011). The focus here is to evaluate MAREANO's (www.mareano.no) geological and geophysical data including multibeam bathymetry and backscatter, shallow seismic, videos and seabed samples, and initial oceanographic (conductivity, temperature, depth, CTD) measurements. We examine the general oceanographic setting, the geomorphology of features such as slope channels, slide scars and glacial debris flows within a sand sink-source context, make inferences from a rigorous dataset

of measurements (metrics) on the bedforms, and synthesize these to suggest an origin and evolution of the sand and bedform fields and the processes driving their formation and mobility.

To date no detailed studies on the SW Barents Sea slope sandwave examples have been conducted. Several fields are present on the slope at a 600 to 800 m depth (Fig. 1). From the outset, the sandwave fields, lying in the path of the northern extension of the North Atlantic Current were recognized as probable manifestations of the geostrophic currents. Further study of the geologic setting and sandwave morphometric studies was undertaken to determine if secondary influence(s) on the sandwaves was revealed, such as topographic focusing, channeled up- or down welling, or internal waves. Furthermore, their spatial coincidence with an oceanographic thermocline positioned them as candidates for influence by (unproven) internal or solitary waves.

2. Bathymetric and geologic setting

The sandwave fields are located on the continental slope in the transition zone between the Norwegian Sea in the west and the Barents Sea in the east. The southern Barents Sea continental shelf comprises alternating shallow banks and deeper troughs formed during the last glaciations (Figs. 1 and 2), and massive diamictic sediments are found (Vorren et al., 1984; Ottesen et al., 2005; Andreassen et al., 2008; Winsborrow et al., 2010). The bank adjacent to the sandwaves in the south, Tromsøflaket, is characterized by N–S-trending, very long and elevated moraines. The sandwave fields are only 1–3 km from the 400 m deep shelf break off Tromsøflaket, but this increases to 6 km in the north.

The Bear Island Trough cuts across the Barents Sea shelf north of the sandwave area, with water depths of 300–400 m, transitioning to the Bear Island Trough Mouth Fan (Fig. 1) in the west (Laberg and Vorren, 1995). At the shelf break, the 100 m high escarpments (Fig. 2) of the gigantic 200,000–300,000 year old Bear Island Slide occur (Laberg and Vorren, 1993).

MAREANO data and data from earlier studies show a surficial sedimentation pattern on the continental shelf influenced by pre-existing glacial features and sediments, bathymetry and ocean currents (e.g., Hald and Vorren, 1984; Vorren et al., 1984, 1989; Bellec et al., 2008; Bøe et al., 2009, 2010; Buhl-Mortensen et al., 2010). Lag deposits

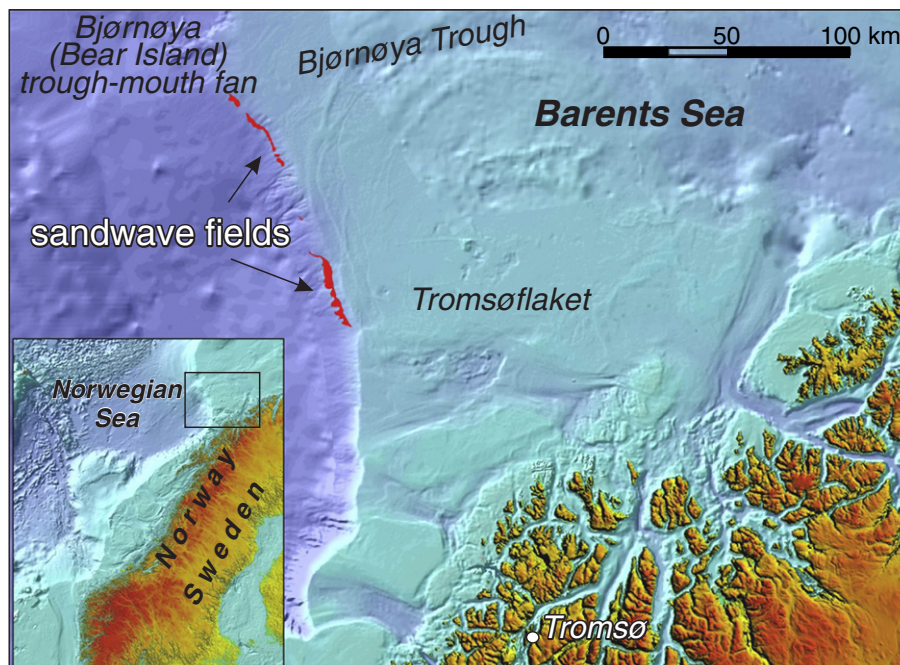


Fig. 1. Location of the sandwave study area on the southwest Barents Sea continental slope. Red areas mark sandwave fields.

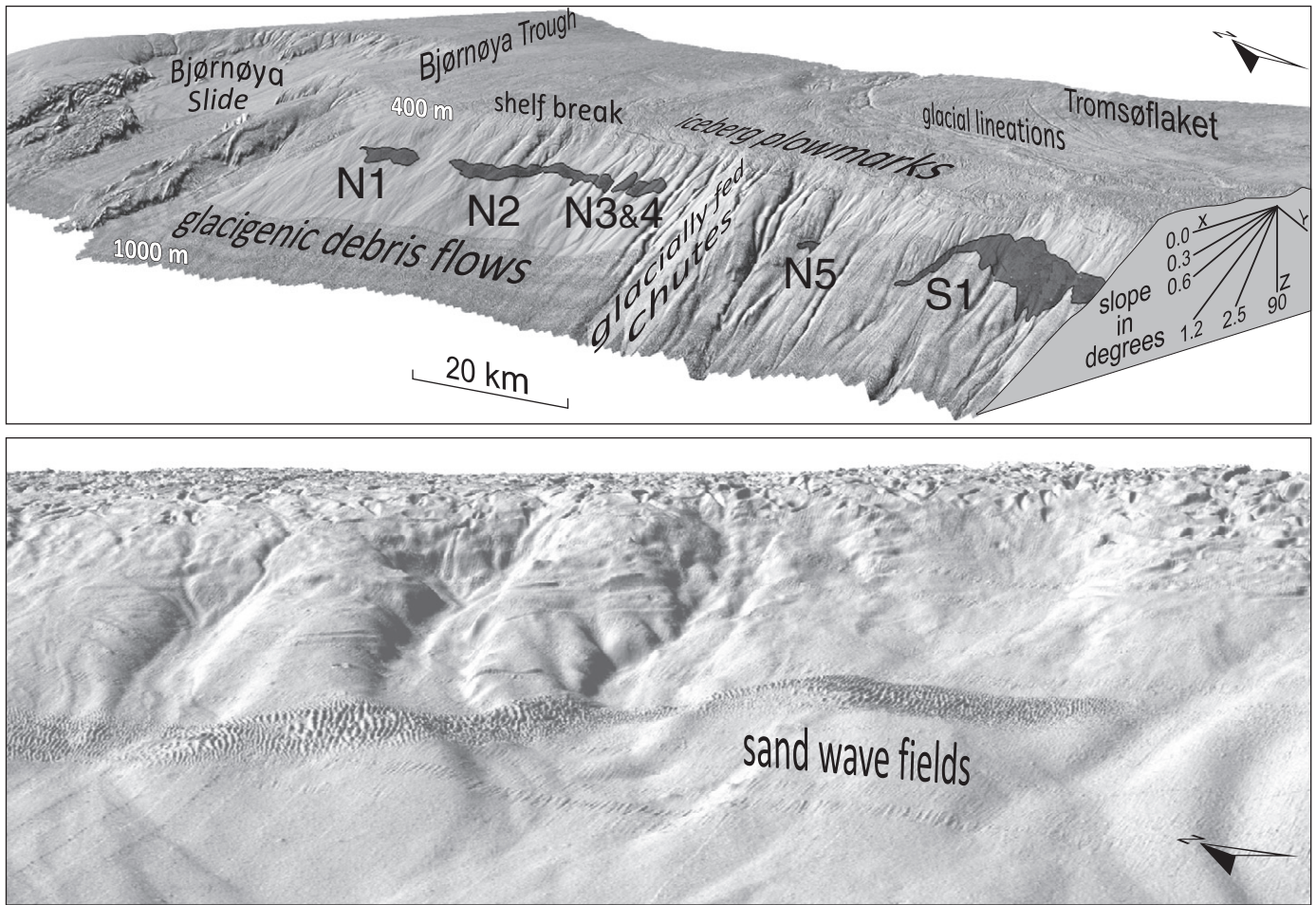


Fig. 2. 3-D rendering of multibeam sonar shaded relief bathymetry showing the general setting of the sandwave fields (dark gray, designated N1 to N5 and S1). These are situated below a glaciated and (relict) iceberg scoured shelf, south of the large Bear Island Slide, and superimposed on multiple canyon-like chutes mainly from glacial processes. The bedforms range from 480 to 750 m water depth. Bottom panel is a closer view and low-angle perspective of the S1 field.

occur on banks and locally on the continental slope (Fig. 3), testifying to the influence of a high-energy environment eroding the glacial sediments. Deposition of fine-grained sediments occurs in troughs and sheltered depressions (Vorren et al., 1984; Michels, 2000). The outermost shelf and just beyond the shelf break have little sand, with the exception of some partially filled iceberg scour troughs. Winnowing by along slope (contour) currents of the upper slope has occurred during interglacial periods (Laberg and Vorren, 1993, 1995). A contourite deposit comprising fine-grained sediments has been described below 1000 m depth south of the study area, on the slope off Lofoten (Laberg et al., 1999; Laberg and Vorren, 2004).

Glaciers advanced through fjords onto the continental shelf, locally developed into ice streams and reached the shelf edge during the last (late Weichselian) glaciation, which reached a maximum slightly before 18,000 C¹⁴ BP. Deglaciation of deep troughs took place from ~15,000 C¹⁴ BP, but ice was grounded on the outer shelf banks for a longer period (Winsborrow et al., 2010). During the middle–late Pleistocene, debris flow activity dominated the slope (Laberg and Vorren, 1995; Vorren et al., 1998; Laberg et al., 2010). The debris flows have unique geometry, lithology and flow characteristics related to their shelf–break situated ice stream source and are termed glacigenic debris flows, abbreviated GDFs (King et al., 1996; Nygård et al., 2002).

In the northern part of the study area, seaward of the mouth of the Bear Island Trough, sub-bottom profiler data show that GDFs occur directly below the seabed sand unit (Fig. 4). These are characterized by a stacked, braided pattern with relief of only meters or less (Fig. 2). In

the south they are blanketed with layered glacial marine deposits, locally up to a few meters thick, in turn covered with thin sand and gravel lags.

There is a marked change from north to south in the presence of downslope channels or gullies with linear, dendritic and anastomosing patterns, both buried and surficial (Figs. 2 and 3). Gullies in the south are typically 20–40 m deep, while they may be up to 150 m deep lower on the slope, where they merge. The gully cuts have lens shaped infilling bodies with the acoustically semi-transparent, incoherent and homogeneous signal characteristic of GDFs (Laberg and Vorren, 1995; Vorren et al., 1998; Laberg et al., 2010). They are interpreted to represent cohesive mass transport, debris flow deposits similar to deposits on the North Sea Fan (Nygård et al., 2002). We interpret the gullies to be formed by debris flow activity (some initiated at sediment slide sites) emanating from the ice margin on Tromsøflaket and term them GDF chutes. The chutes are usually, but not exclusively, devoid of a capping glacial marine blanket (Fig. 5, position a) in contrast to the more continuous blanket over GDFs outside the gullies. It is unclear if this represents GDF activity synchronous to the interfluvial glacial marine blanket (and assimilation) or later (current) removal. The thalwegs are occasionally sandy at the immediate seabed, contrasting with ubiquitous gravel elsewhere.

Thus, cold and dense glacial margin-derived meltwater could have been instrumental in some of the chute history. Vorren et al. (1989) recognized these chutes (gullies) but attributed an interglacial cold (winter), dense shelf water and downslope transport process (cascading) on the basis that they are basically sediment-free (bypass

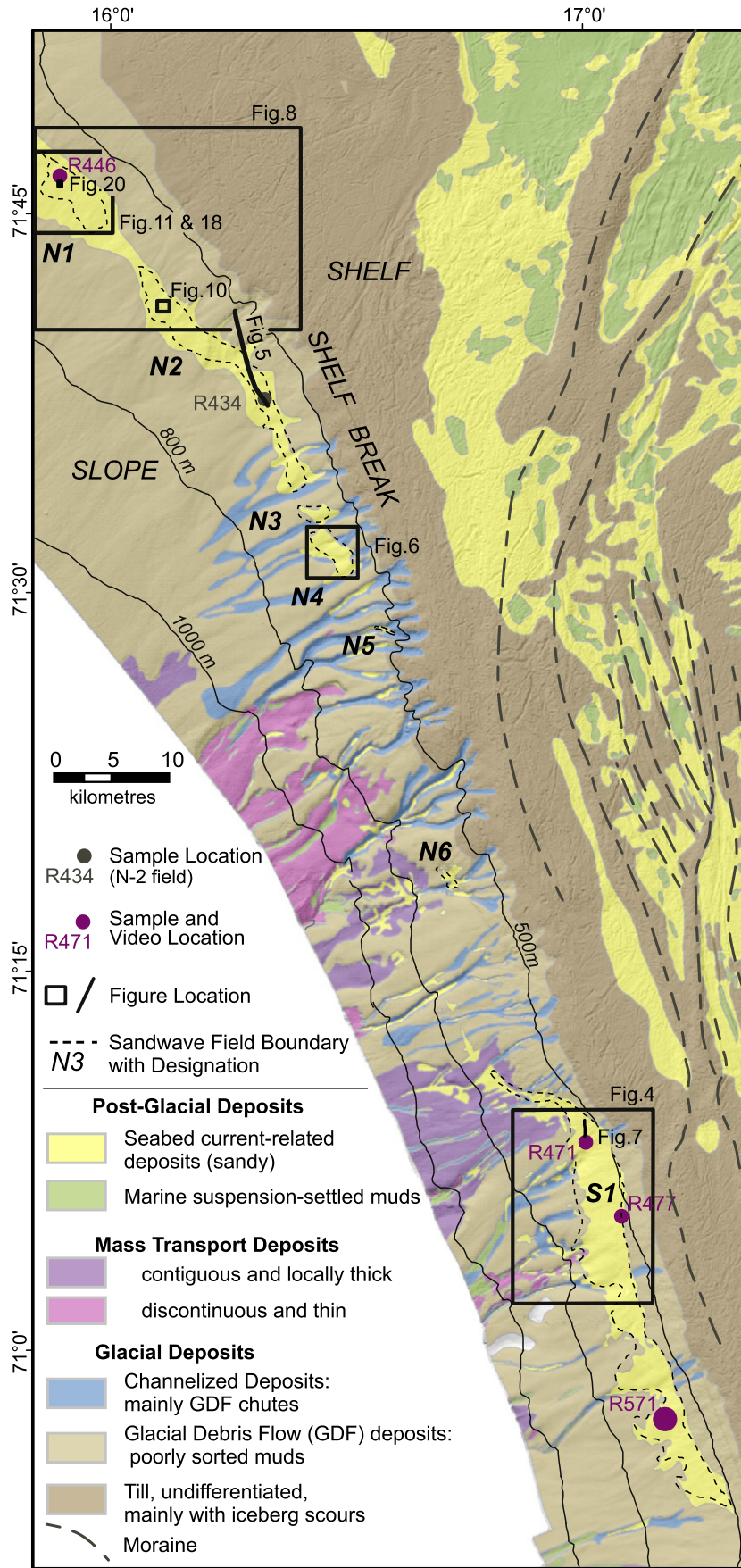


Fig. 3. Outline of the sandwave fields in the context of the MAREANO surficial geology (genesis) map (Bellec et al., 2012a and b). Also shown are sample, video, map and seismic illustration locations.

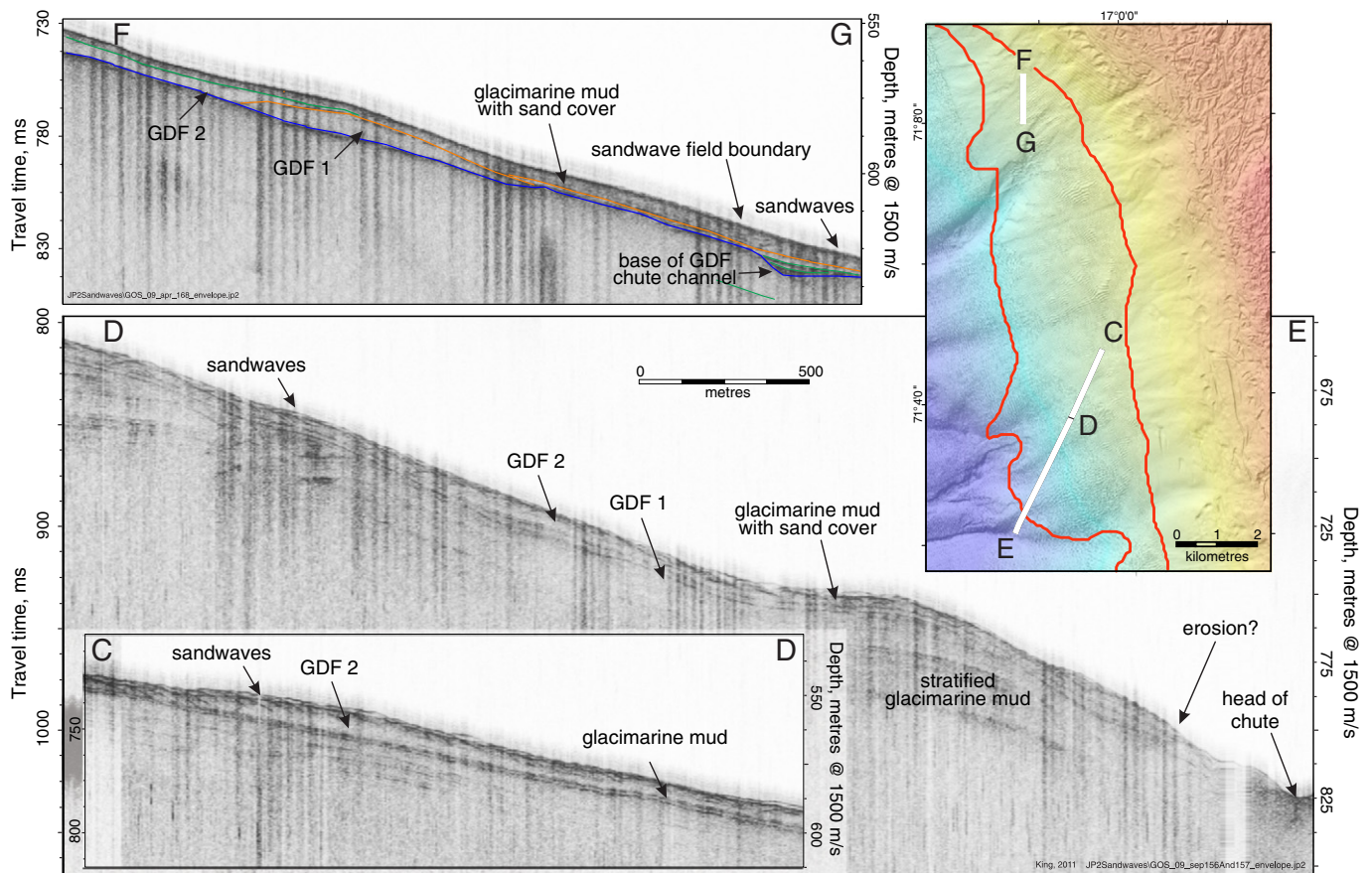


Fig. 4. Topas sub-bottom profiler transect across the S1 sandwave field. The lower panel (C–D) connects with the larger (D–E). Small sandwaves lie on top of stratified glacimarine sediments. See Fig. 3 for location.

sites). This is also the interpreted transport mechanism for long-term feeding of muddy contourites off the Spitsbergen margin (Rudels et al., 1999), but inferred during glacials. The 1989 work predated recognition of the GDF phenomenon and utilized low-resolution seismic, unable to resolve them in the partially filled gullies. The Spitsbergen work recognized intercalation of drift horizons and GDFs, much like observed here (Fig. 5, positions b and c). Cold and dense glacial margin-derived meltwater could have been instrumental in occasional removal or preventing deposition of the glacimarine blanket in the thalwegs. A limited post-glacial sandy downslope transport is considered in a later Section (6.3).

Several large, submarine slides of poorly constrained age have occurred in the central and southern parts of the study area but are mainly covered by debris flow deposits and glacimarine sediments and present little seabed expression. Smaller slides with good seabed expression are scattered over the study area. At least 23 slides were identified within 10 km of the sandwave fields. These range from 0.5 to 4 km² and cut glacimarine sediments, post-dating the GDFs (Fig. 6).

The sands comprising the sandwaves lie on top of the GDFs or the glacimarine blanket (Fig. 7). They are invariably thin, the majority of sand within the sandwave itself, and it is common that the sandwave troughs coincide with the gravel lag marking the top of the glacial sediments.

3. Oceanographic setting

The North Atlantic Current (NAC) (Norwegian Atlantic Current, NwAC along the Norwegian margin) carries warm and saline North Atlantic Water (NAW) into the Nordic Seas (Fig. 8). The NAC splits in two branches west of Tromsøflaket. One branch follows the continental

slope north–northwestwards toward Svalbard, while one branch swings into the Barents Sea. The Norwegian Coastal Current also flows north, along the coast (Rudels et al., 1999).

Three well defined water masses are differentiated offshore Lofoten–Vesterålen–Troms along the NW Norwegian continental slope (e.g. Helland-Hansen and Nansen, 1909; Hopkins, 1991; Hansen and Østerhus, 2000). North Atlantic Water (NAW) is characterized by salinity > 35, and is typically found on the upper slope shallower than ca. 700 m depth. NAW has temperatures above 6 °C at the mid-Norwegian margin (Haugan et al., 1991) and flows northeastwards along the slope with typical current speeds of 0.2–0.4 m/s (Heathershaw et al., 1998) but occasionally reaching surface velocities in excess of 1 m/s west of Lofoten and Vesterålen (Poulain et al., 1996). Norwegian Sea Arctic Intermediate Water (NSAIW) occurs at ca. 700–1000 m depth with temperatures between 0.5 °C and –0.5 °C and is less saline than the water masses above and below (Hansen and Østerhus, 2000). Norwegian Sea Deep Water (NSDW) occurs below ca. 1000 m with temperature below –0.5 °C (Hansen and Østerhus, 2000). The depth of the transition zone between the water layers varies throughout the year, deepening in the winter, and long wavelength internal waves may occur.

4. Methods

The study area (Fig. 1) was mapped by multibeam echosounder (Kongsberg Simrad EM710, 70–100 kHz range) by the Norwegian Defence Research Establishment/Norwegian Mapping Authority in 2008–2009 as part of the MAREANO program. The multibeam echosounder provides two datasets: bathymetry and backscatter. The backscatter (acoustic reflectance) is influenced mainly by sediment

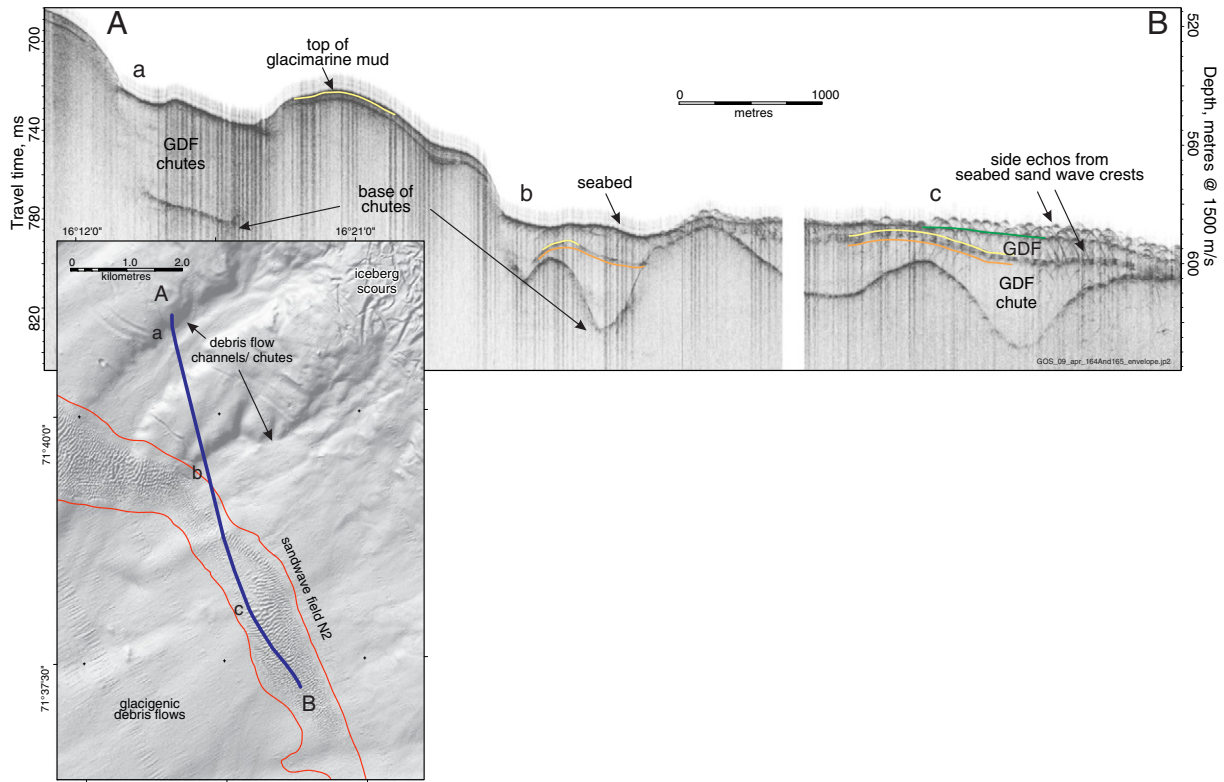


Fig. 5. Topas sub-bottom profiler longitudinal transect across the N2 sandwave field. GDF-filled channels (e.g. positions a and b, flow tops locally shown in orange) are overlain by a blanket of glaci-marine muds about 3 m thick (top shown, yellow). It is locally covered with subsequent GDFs just beneath the sandwaves, their base locally marked in green. See Fig. 3 for location.

texture in the uppermost 0–30 cm of the seabed, and gives information on hardness and roughness. Backscatter data were processed via GRASS 5 software using beam correction and intensity normalization tools developed by the Geological Survey of Canada-Atlantic. Hard/rough bottoms (bedrock, coarse or compacted sediments) generally show higher backscatter values than soft/flat bottom (mud, uncompacted sediments). The data density was sufficient for gridding at 5 m, allowing detailed analysis of seabed features but no resolution of superimposed bedforms (seen in video coverage).

Sub-bottom profiling utilized a parametric sonar (TOPAS) from Kongsberg Maritime, a hull-mounted source centered on about 3.7 kHz, filtered and heave compensated. Vertical resolution exceeds 1 m and penetration is generally 20 to 30 m in the sand-covered glacial sediments.

A transect of conductivity, temperature, depth (CTD) casts was performed across the upper slope and shelf break near one of the sandwave fields on April 19th 2011 with R/V Helmer Hanssen. The DIVA Gridding method of the Ocean Data View software (Schlitzer, 2012) was used to interpolate the temperature and salinity data for identifying the water masses in the study area (Fig. 8).

Seabed sediment samples, video transects and the shallow seismic data were acquired during MAREANO cruises with the research vessel G.O. Sars in 2009–2010 to calibrate the multibeam backscatter data, and for biological, geological, and geochemical sampling and analysis. Sampling for biological and sedimentological studies was performed by grab, boxcorer, epibenthic sledge and beam trawl. The video surveys were performed using the Institute of Marine Research's towed video platform CAMPOD, which is a metal-framed tripod equipped with low light CCD overview camera and a high definition (HD) video camera. Further details on the CAMPOD and its operation are given in Bellec et al. (2008), Dolan et al. (2009) and Buhl-Mortensen et al. (2009).

4.1. Data processing and bedform analysis technique

The seismic data were interpreted using a publicly available GSC desktop seismic software package (Courtney, 2007) based on SEG Y and efficient JPEG 2000 technology. For sand thickness distribution, horizon picks were readily exported as seabed to base of sand deposit to GIS (ESRI ArcMap 10) shapefiles.

Derivatives of the multibeam echosounder bathymetry grid included 3-D rendering, crestline tracing, seabed slope and statistically robust bedform metrics. Most analysis involved derivation of sandwaves morphometrics from the bathymetric grid to fully characterize the forms with a regional topography setting. The objective was to assemble a suite of derivative bedform metrics attributed to spatially preserved trough positions for viewing and statistical analysis in GIS. This was accomplished through a combination of extraction, filtering, auto-picking of troughs and crests and subsequent filtering in both ArcMap and spreadsheet (Excel) environments.

Six individual sandwave fields were outlined and designated north (N) and south (S) and numbered sequentially (N1–N5 and S1, Fig. 2). To sub-sample the 5 m gridded bathymetric digital elevation model, water depth profiles were extracted with elevation values for each 5 m along crestline-normal transects spaced at 100 m and fully covering each field. Eleven zones of such transects were generated (e.g. one for the S1 field, five for N2; a to e, etc.) to best align the profiles normal to the crestlines. There is sinuosity, of course, in the crestlines and accordingly some variation from the normal arose. This affects (slightly diminishes) true sandwave flank slope values (though ratios, such as asymmetry, remain valid). Deviation from the transect orientation was typically 10° to 15° (one SD) relative to the transect. The extracted depth values (with associated UTM coordinates) along all such profiles were assembled in spreadsheets. An auto-picking routine was developed to recognize minima and maxima (troughs and crests). The

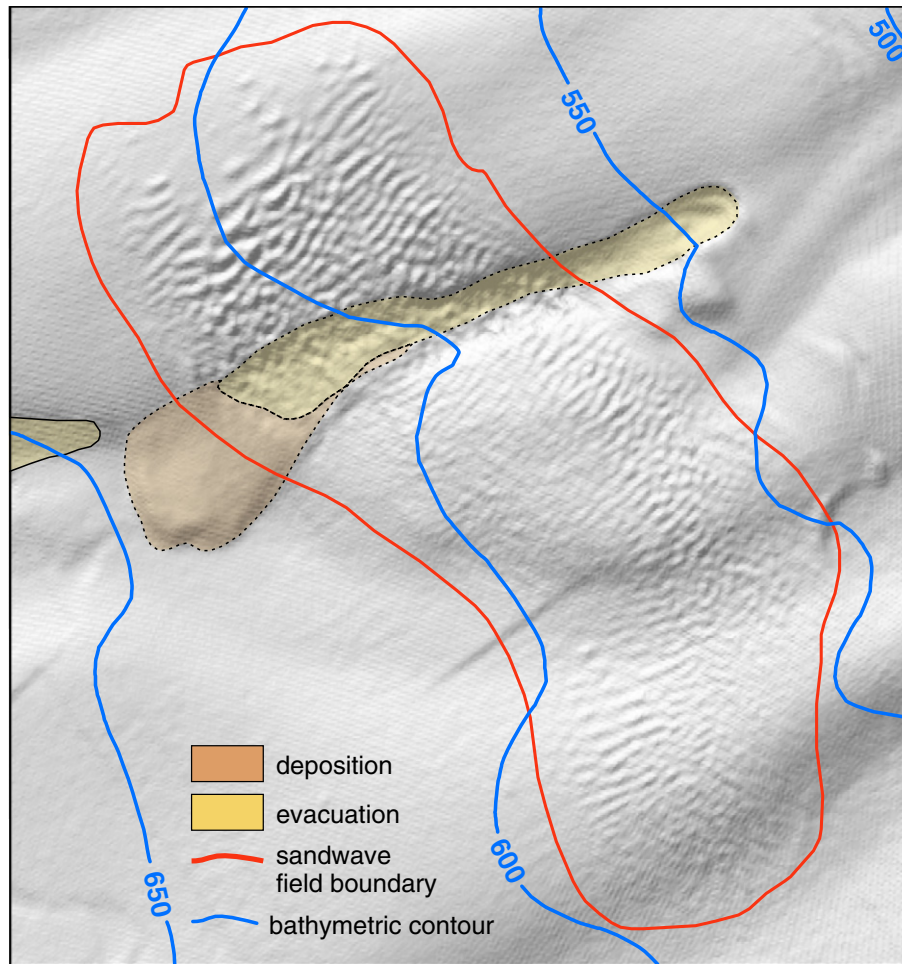


Fig. 6. Post glacial slide in field N4 showing evacuation and deposition slide elements. Most such failures involve both GDFs and glacial marine deposits. The sandwaves cross the feature, unaffected. See Fig. 3 for location.

profiles were smoothed slightly using a Hann filter to minimize small perturbations, presumably both noise and superimposed bedforms, whose measurement locally excluded recognition of the larger (>2 m high) bedforms in the auto-pick function. The auto-picked values were filtered to eliminate remnant low amplitude (<10 cm) and very

short and long wavelength forms ($10\text{ m} < \lambda < 1000\text{ m}$) which represented noise and small-scale glacial debris flow channel flanks respectively. Smoothing and metric derivatives and definitions are shown graphically in Fig. 9.

These measurements provided the basis for robust statistics of the bedform metrics, including height, wavelengths, profile symmetry, and stoss and lee flank slope, slope ratio and crest and trough sediment texture. All measurements (approximately 30,000 bedform profile samples) were assembled as GIS attributes (fields) for each data point trough location X–Y coordinate (UTM Zone 33) such that their spatial distributions within and among the fields could be investigated following re-entering the spreadsheet values in the GIS environment (Fig. 10).

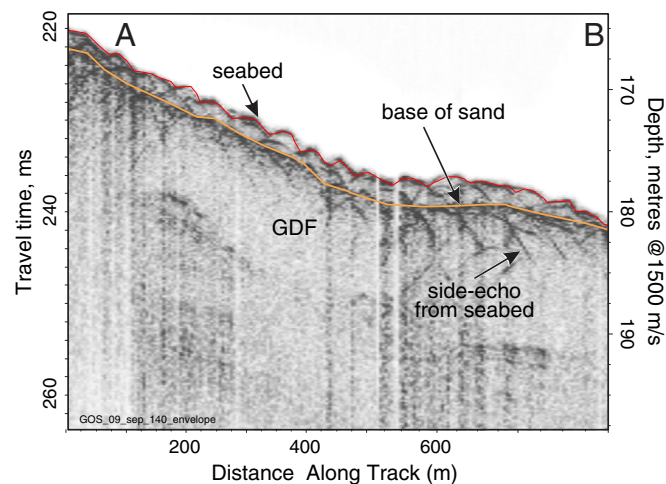


Fig. 7. Topas sub-bottom profiler transect across the northern area of the S1 field. The relatively steep bedform faces create hyperbolic side-echo artifacts. The base of the sand field is glacially-derived diamicts and stratified muds. Sand here is 1–4 m thick while bedform amplitude is about one meter. See Fig. 3 for location.

4.2. Data resolution and limitations

A small percentage of auto-pick “misses” relate to the larger bedforms (Fig. 10, open arrows in lower panel) either where they are compound (near crestline bifurcations) or have smaller, superimposed bedforms. This was deemed to occur so seldom as to have little statistical effect but it would skew the maxima slightly.

Although seabed video observations are not quantifiable in terms of bedform height, wavelength, slope, or compass orientation, the impression from derived photographs is that lee slopes are steeper than that measured from the multibeam. Slopes were measured from the extracted profiles (Fig. 9), generated at the same grid resolution as the multibeam grids such that values would match GIS-generated slope displays. Lee-slope crest to trough distances in video photographs appear

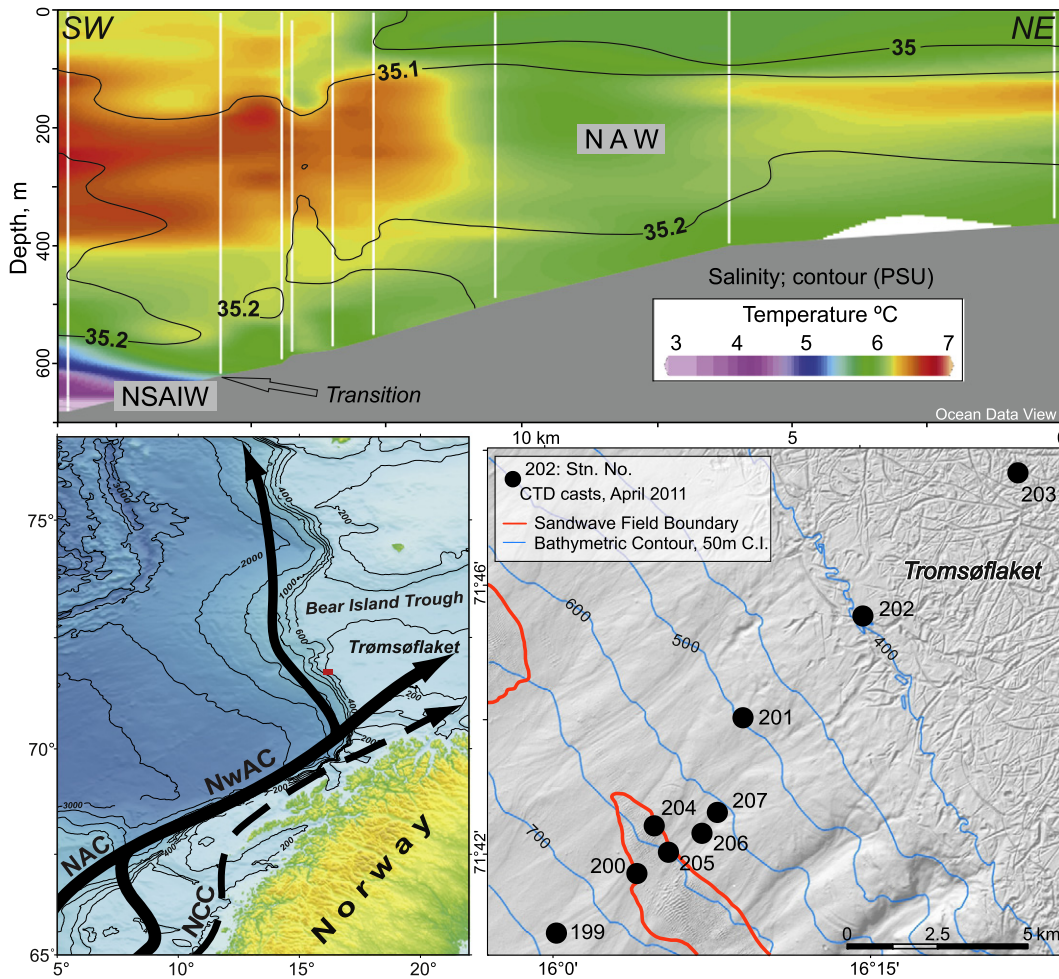


Fig. 8. Oceanographic setting at the sandwave fields. Lower left panel shows stylized components of the North Atlantic Current (NAC), the Norwegian Coastal Current (NCC) and the Norwegian Atlantic Current (NwAC). Red box blow-up, lower right shows location of a series of nine CTD casts (April 2011) in relation to the sandwave fields (location in Fig. 3) while the upper panel shows temperature and salinity from those casts (white vertical lines are the CTD locations). Note the transition depth between North Atlantic Water (NAW) and Norwegian Sea Arctic Intermediate Water (NSAIW).

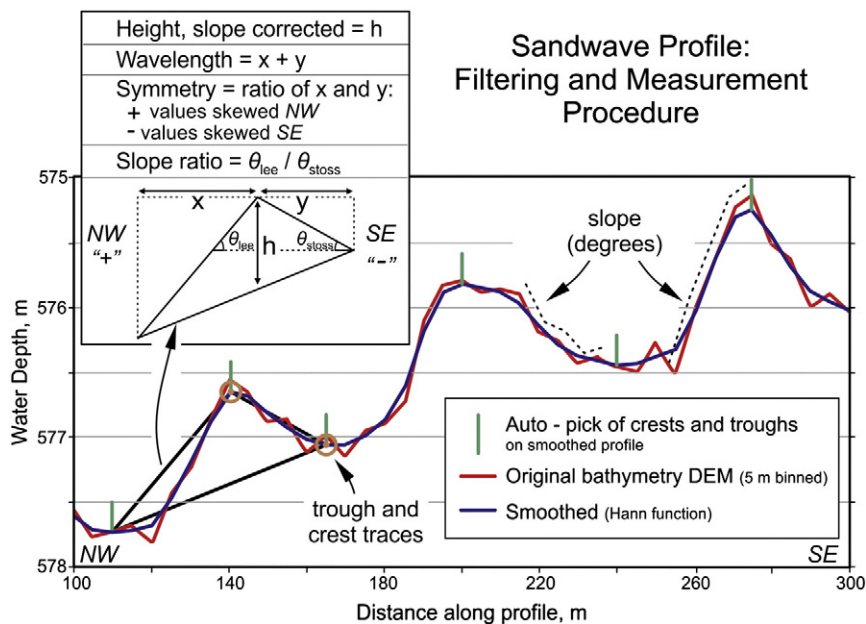


Fig. 9. Bathymetric profile of sandwaves in the N1 field demonstrating derivation of the metrics. Profiles generated normal to the sandwaves at 100 m spacing (red) were smoothed (blue). Crest and trough elevations and coordinates were auto-picked and further attributed with a variety of morphometric parameters.

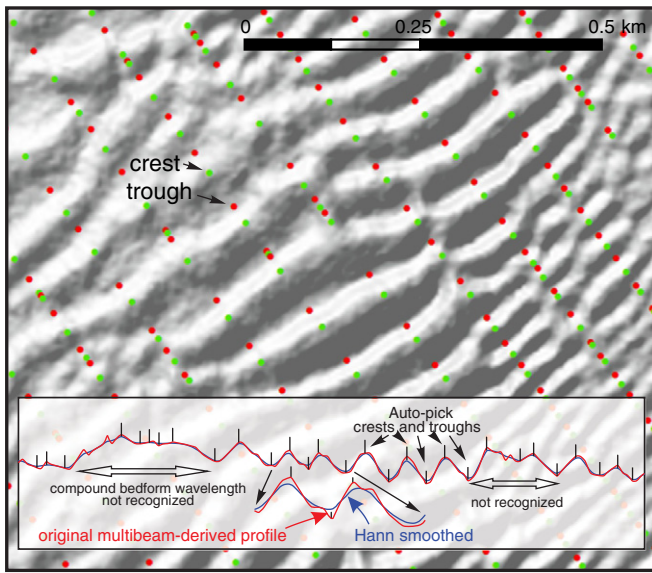


Fig. 10. Shade relief showing spreadsheet-derived auto-pick results for recognition of bedform troughs (red) and crests (green). Vertical lines mark the auto-pick generated points on the profile panel and the corresponding pick locations on the shaded relief map (in GIS). Open horizontal arrows (lower panel) highlight large forms not recognized with the auto-pick. The trough sites were assigned the morphometric attributes noted in Fig. 9.

to be several meters only; this is less than the 5 m gridding resolution of the multibeam which is constrained by acoustic spreading through the over 600 m water column. A 20° slope on a 2 m high hypothetical sandwave, for example, has a crest to trough distance close to the 5 m grid resolution and could be registered correctly if acoustic “pings” happen to be grid-sampled at the top and base of the lee slope. Yet the worst case scenario would yield a slope measurement of only 7° on such a bedform (mid stoss and mid lee ping samples). This situation worsens, of course, with slopes greater than 20°. Only 0.1% of measured slopes exceed 20° in this compilation. This does not necessarily negate the slope ratio index or the symmetry indices, which are relative measures, but it is clear that smoothing due to acoustic spreading sets serious limitations on small, angular seabed features such as observed in the video.

The outcome is that absolute slope and symmetry measurements (and their ratios) from the multibeam data represent “flatter” bedforms than in reality. The 5 m grid limitation has less serious implications for height and wavelength measures and their metric derivatives but robust statistics should still yield significant and credible trends. Low resolution gridding has obvious implications for future serial surveys if migration rates are less than or close to 5 m between surveys.

5. Sandwaves and sandwave fields

5.1. Shape, composition and superimposed ripples

Fig. 11 shows a detailed example of the slope-situated sandwaves. These are small to mid-scale 2-dimensional with occasional bifurcations. They are generally largest in one or more centralized domains and diminish in height and wavelength toward the field boundaries. Some curvature of the crestlines is attributable to swings in the trends of underlying topography.

Orientation of the sandwave crestlines (Fig. 12) from manual traces of the multibeam image shows a strong SW–NE trend, normal to the trend of the local bathymetric contours. Crestline orientations are consistently normal to the regional slope $\pm 10^\circ$ SD. Notably, crestline orientations are more tightly grouped than the bathymetric contours. Deviations of the contours from the NW–SE trend are related mainly

to the meso-topography of slope-parallel glaciogenic debris flow chutes. This illustrates a relative insensitivity of bedform orientation to these chutes as seen in Figs. 2 and 11.

In profile, the sandwaves can be quite sinusoidal with symmetric or slightly asymmetric stoss–lee relationships as measured from the multibeam sonar grids but, as explained in Section 4.2, this is a much smoothed dataset, not capable of resolving steep slopes. The video transects show a long stoss (southern) face with imperceptible slope (no slope or instrument orientation measurements were possible) and a very sharp crestline with a steep lee side oriented downstream, where possible to discern.

An overview of sediment composition is derived mainly from acoustic backscatter. The acoustic return from outer-beam transducers (those at low seabed incidence angle, outside about 20°), is sensitive to scattering, with stronger signal for rougher seabed. Gravel generally results in a stronger backscatter signal than sand and several 800 m long video transects across the bedforms confirm this (following paragraph). The data are plagued with noise (recognized in ship trackline patterns) but backscatter strength spans almost 50 dB across the region and is generally about 10–20 dB lower within the sandwave field than the surrounding gravel/cobble lag seabed. Sandwave troughs are frequently gravel floored where the sand thins sufficiently to expose a larger expanse of the basal gravel (Fig. 11, panel C). Analysis (not shown here) demonstrates little or no net difference between crests and troughs on a whole field basis, partly because the troughs on the smaller, flanking sandwaves do not often reach down to the lag, and partly because the backscatter noise is often as strong as the crest–trough variation.

Seabed samples, though limited, confirm the seabed texture from acoustic backscatter. Grab samples (R571, location Fig. 3) from the southern S1 field, yielded gravel at a trough site and sand from a lee or stoss setting. A nearby box core recovered a few centimeters of well sorted sand and a multicorer (short gravity core-type carousel) recovered 10–15 cm sand, gray on top transitioning to olive gray at 2 cm depth, with clear concentrations of the denser (dark colored) minerals associated with ripples. These were sub-sampled (seven 1 cm thick slices) for further grain size analyses which yielded 100% fine to medium sand. The N2 field (R434) yielded small grab and box core samples of fine to medium sand, the former with traces of the coarse sand size shell hash which concentrates in the sandwave lee sides and ripple troughs. In the northern S1 sandwave field (R471, Fig. 3), grab and box core samples yielded up to 17.5 cm of fine sand.

A variety of ripples, superimposed on the sandwaves, are visible in the video-derived photographic stills. Fig. 13 shows views of the lee edge of some sandwaves, emphasizing abrupt changes in superimposed ripple shape and crestline orientation. The sandwave crest and stoss typically have complex 3-D ripples (generally linguoid, panel A) with swirled patterns arising from sorting of shell hash and dark heavy minerals. Current sense from the strong asymmetry and ripple shape (A, C, and F) is, as expected, generally normal to the crestline trend of the sandwaves. No clear stoss- to lee-flank grain size difference is recognized.

A remarkable change in superimposed ripple type and orientation generally occurs at the sharp crest of the sandwave. Fig. 13 (C, E, and F) shows three examples. The lee-face superimposed ripples are 2-D with very linear crests and occasional bifurcation. They are asymmetric and have crest orientations highly oblique to the sandwave crestline, occasionally almost normal. The contact between the two ripple types is abrupt with one “blending” to the other over less than 10 cm. The transition is a cross-cutting relationship where the newly-formed set appears to anchor to an existing crest, cannibalizing it. Clearly, shell-hash floored ripples at the base of the sandwave slip-face at Station 446 (Fig. 13, C and E) allow recognition of an asymmetry indicating transport direction to the photograph’s left. Comet marks behind trough-situated cobbles from other photographs (not shown) confirm this. We cannot be certain if this represents regional up-slope or down-slope ripple migration; the remote video Campod navigation

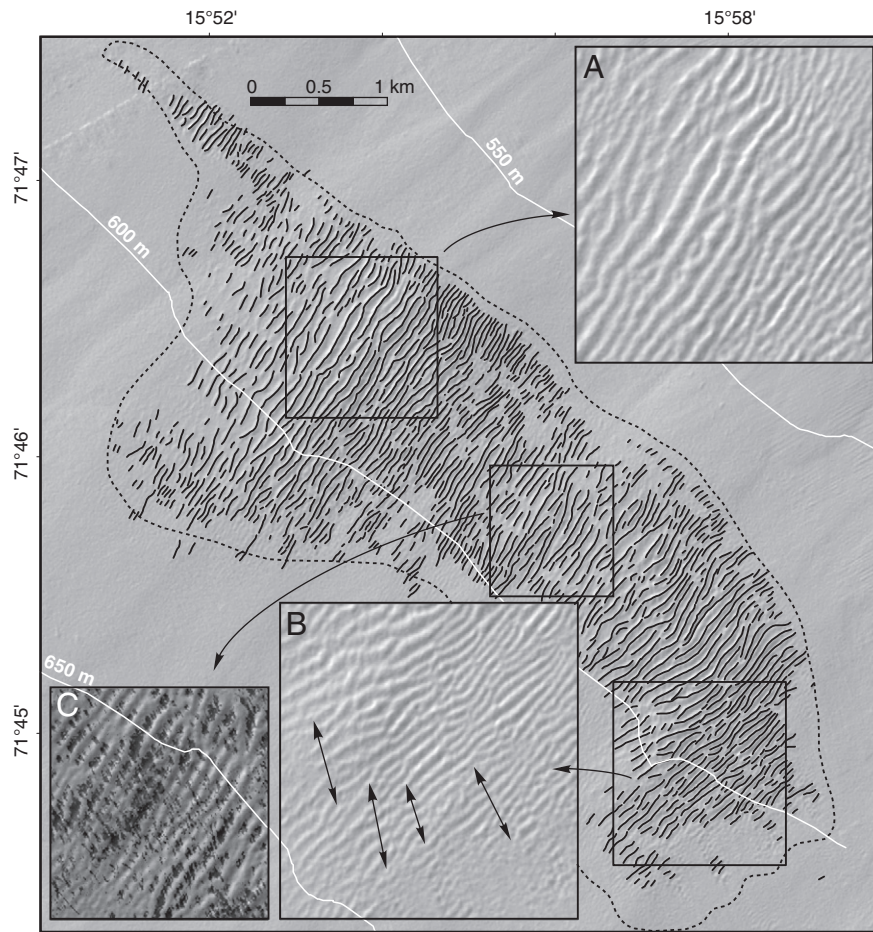


Fig. 11. Shaded relief multibeam echosounder image (illumination from NW) showing pattern of sandwave crestline traces for the N1 field (white bathymetric contours in meters). Inserts A and B show details without traces. Double arrows align with flow-parallel elements marking subtle discontinuities in the crestlines in insert B. Insert C shows acoustic backscatter strength over the shaded relief image (darker is higher backscatter; more gravelly). See Fig. 3 for location.

was unreliable for much of the transect and the ROV did not have orientation sensors. However, profile asymmetry measurements from multibeam data (following Section, 5.2) demonstrates that 85% of the sandwaves along this video transect display a neutral or NW-facing lee face (remainder to the SE). This indicates a good probability that these lee and trough-situated ripples demonstrate local upslope migration.

In summary, sharp-crested sandwaves oriented slope-normal and with lee-face to the north are composed of fine to medium sand with shell hash, more prominent in the troughs. Some troughs bottom in a basal glaciogenic gravel lag. Superimposed ripples are ubiquitous and periodically active. The abrupt contact in ripple type and orientation at the sandwave crest indicates that at least two different and successive current processes can be inferred, one a contour current and the other a regional up-slope (and possibly corresponding down-slope) component.

5.2. Sandwave morphometrics

Sections 4.1 and 4.2 described derivation of sandwave metrics from multibeam sonar and their limitations. Various indices were generated to identify if morphology could point toward sediment processes. Results from this analysis are presented here. Table 1 summarizes field dimensions, height and wavelengths and symmetry. Table 2 summarizes bedform slopes, acoustic backscatter and sand source and sink volume estimates. Some of these parameters are also presented graphically in Fig. 14. Fig. 15 shows sandwave water depth, height and wavelength frequency distributions. The water depth mean at about 600 m

(596 ± 42 , Fig. 15a) is spatially coincident with the contact and depth range variation between NAW and NSAIW (Fig. 8).

Sandwave heights show a uniform exponential (normal) distribution with an average of 0.75 ± 0.62 m (Fig. 15b). This is compatible with the video observations. Wavelengths (Fig. 15c) are similarly exponentially distributed (tail less than 30 m wavelength is likely due to limited sampling resolution). They are on average 39 ± 16 m across with maxima in the 130 m range. Bedform size varies strongly within the field, mainly in an along-slope sense. Domains of the larger examples fall along the central axis of the sandwave fields but they also have some spatial affiliation with the larger changes in topography, generally near the flanks or on the interflues of the GDF chutes/channels but this is not always the case.

The ratio of height to wavelength (H/L) is a common index of morphometrics and generally considered a rough proxy for bedform activity level (Flemming, 1980; Dyer, 1986). Fig. 16 shows this index for all fields, presented both as a height vs. wavelength plot (a) and as a frequency distribution of their ratio (b). The plot (a) has a columnar appearance due to the 5 m gridding of the original multibeam echosounder grid. Note that the bulk of measurements overlap in the lower left of the plot (the smaller forms) and their density is partially obscured. Dotted lines mark the extremes at 5.5 m height and 210 m wavelength. Fig. 16b shows the frequency distribution of H/L. Significance of the plots is considered below.

Bedform symmetry is a commonly used indicator of sandwave activity and direction of migration where long, low-sloped stoss (upstream) flanks combined with short, steep-sloped lee flanks yield highly asymmetric indices with clear mobility. Fig. 17 shows summaries of

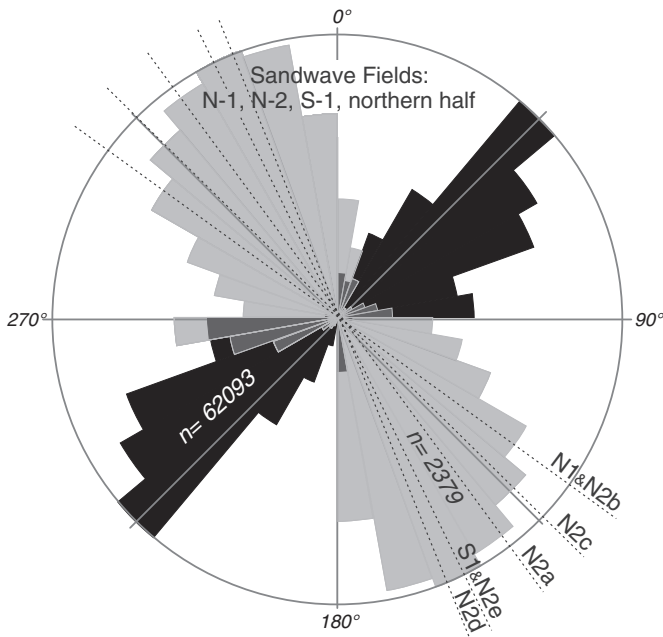


Fig. 12. Rose plot of the crestline orientations of many of the sandwaves (black) in relation to the general bathymetric contours (gray). Transect profile orientations for the measured sandwave fields and sub-fields (a to e) shown as dashed lines. Crestline trace measurements are for each 150 m long segment of a manual trace of the crest. Similar segmentation applies for the bathymetric contours. Number of segment measurements in italics. Orientations are strongly constrained to attitudes normal to the contours, consistent with contour current-driven bedforms.

symmetry and slope measurements. Despite many locations with examples to the contrary, Fig. 17a shows that NW-facing slopes are marginally steeper than SE, considering the entire dataset. Together with the symmetry measurements showing the same, though slight trend, this is interpreted as a general northwesterly preferred migration direction.

Though bedform symmetry shows only weak overall trends where whole fields are considered, most fields exhibit geographic domains which are systematically spatially related to the topography of the GDF chutes. This also imparts a confidence in the asymmetry measurements, despite the shortcomings noted in Section 4.2 because neither survey parameters, water column properties nor processing procedures could create such trends related to the chutes. Fig. 18 shows symmetry distribution across the N1 field (a) and two selected profiles (b) which accent the symmetry-skewness relation to the GDF chute flanks. The shaded relief image is optimized to highlight local slopes of the pre-existing GDF chutes and interflues manifest as downhill-oriented banding demarcated with small, white arrows at the thalwegs. SE-facing slopes of the chutes have superimposed sandwaves with an asymmetry (skewness) in blue tones, indicative of up-hill migration in a downstream (NW) direction. However this pattern is mirrored in the NW slopes, where a green tone indicates up-hill skewness but inferred migration here is in an apparent upstream direction. This manifests as banding in the blue and green dots (panel a) following the GDF chutes. The strongest trends are associated with the smaller bedforms flanking the field; the larger are more symmetric. Similar patterns (not illustrated) were found when NW to SE flank slope ratios were mapped, these emphasizing actual lee and stoss slope differences as opposed to the symmetry index.

Another aspect of symmetry was examined by comparing frequency distributions in the N1 field for a range in classified sandwave heights. The hypothesis was that large bedforms, with large sand volumes, might have longer response time lags to variations in current direction than the smaller forms and thus better reflect an expected dominant long-term northeasterly flow direction. Fig. 19 shows bedform size

relationship to symmetry direction. Symmetry frequency distributions for five classes of bedform heights are compared. Median symmetry values are about +0.16 for all classes of bedform heights combined, compatible with the overall northwestward (general downstream) migration established earlier. The highest bedforms (>1.5 m) display a much stronger asymmetry, most with northwestward (downstream) skew but with a clearly separate population displaying southeastward skew. The progressively lower height sandwaves, though still slightly skewed to downstream directions, include increasingly greater numbers of southeastward (upstream) skews. These observations suggest that rather than large bedforms showing a time-averaged northeasterly flow, as hypothesized, they preserve real and opposite yet relatively stable (long term) net current directions. Furthering this interpretation, the smaller forms likely react more quickly, reflecting variability of the current directions at their respective response capabilities.

6. Sandwave field formation and maintenance: sink, source and age

6.1. Sandwave field volume

The base of the sandwave sand was traced on all available TOPAS transects across the fields but distribution is inadequate for a complete sand volume assessment. Generally, troughs of the larger examples, centrally located in the fields, expose basal gravel lags while the flanks of the fields are continuous but thin (<1 m) sand. Given inadequate seismic coverage, volume estimates were calculated based on sandwave half-height measurements. The latter were based on a simplified model of adjoining trochoidal shaped sandwaves whose troughs reach the underlying immobile gravel. Height and wavelength statistics from the 100 m spaced transect profiles generated from the multibeam bathymetry were used to generate these volume estimates for each field (Sink Volume, Table 2). This technique suggests about $50 \times 10^6 \text{ m}^3$ of sand in the S1 field, $15.7 \times 10^6 \text{ m}^3$ in N2, and ranging from 0.1 to 3.9 for the other fields, for a total of about $72 \times 10^6 \text{ m}^3$ (0.07 km³).

6.2. Sand source from winnowing

The only present day sand accumulation, apart from the sandwave fields, is extensive, irregular patches of sand and gravelly sand veneers over till on the shelf, (Fig. 3). These sands derive mainly from the sand component of the underlying glacial diamict through erosion by current winnowing as seen elsewhere (Vorren et al., 1984; Laberg et al., 1999; Laberg and Vorren, 2004). There are no specific sand transport pathways to the slope evident in the present day sand distribution, except at the surface of the deeper part of GDF chutes but clearly the iceberg scoured, lag-covered till exposed here suffered winnowing and most of the fine sediment component was removed.

Above the shelf break this sand would have been largely till-derived but below the break the surficial sediment is primarily the GDFs and the stratified glacial marine sediments (Figs. 3, 4 and 5). These would be more subject to current erosion than the harder till but all varieties eventually develop a protective gravelly lag with only (early stage) iceberg scour turbation contributing “fresh” surfaces. Direct observation of winnowed lag is also clear in the seabed videos. Lag thickness is often limited to a mono-layer as evidenced by occasional fishing trawl cuts. An erosion thickness estimate from the sub-bottom profiler data is poorly constrained because amounts less than one meter would doubtfully be recognized in non-stratified sediments and would only be recognized in stratified sediments if it produced an angular unconformity rather than a disconformity. A winnowing source hypothesis for the sand seriously limits the volume of locally-generated sand.

6.3. Slope bypass of sand

The GDF chutes generally contain muddy mass transport deposits from glacial processes. How much post-glacial sand might they have

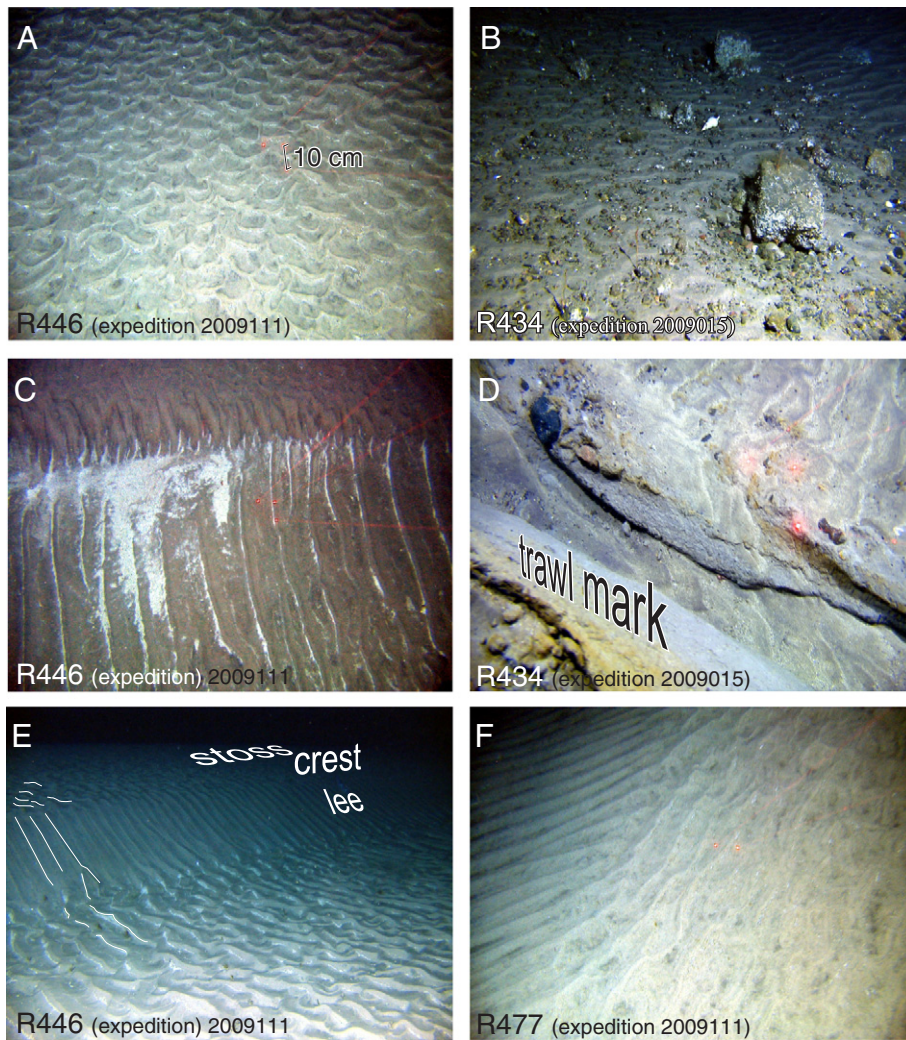


Fig. 13. Photographic stills from video transects across the sandwaves (10 cm between red lasers). Crests highlighted in lower left. Locations of R-stations, Fig. 3.

directed to the base of slope? Data coverage at the base of slope is not available so identification of sandy lobes or sheets, if any, is not yet possible.

Though not measurable from sounder profiler, the acoustic backscatter proxy used for the surficial texture mapping in Fig. 3, together with the video tracks, indicate a discontinuous, thin gravelly sand cover in the some thalwegs, often worked into ripples. The same phenomenon is observed at a smaller scale outside the chutes; linear trawl marks (scours from fishing activity in the area up to decimeters deep) observed on video have subsequently trapped sand. Thus, modern sand traction occurs, at least locally. It does not, however, confirm slope bypass; nor does it prove unidirectional transport.

The area of the N fields has a sand distribution restricted to the water depth range of the sandwave fields, i.e. not preferentially along the chutes (Fig. 3). Also, the sandwave crestline patterns continue, apparently uninterrupted, across the chutes. This suggests that if any appreciable sand deposit has been captured (trapped) in the chutes, it is through a contour current process rather than via a down-slope conduit.

The northern third of the S1 field and immediately north is somewhat exceptional because here sand distribution is broader than the sandwave fields (Fig. 3). Here sand-filled iceberg scours extend to the shelf break and at least five down-slope chute systems have significant, though generally not continuous bands of sand following their thalwegs. There is no clear spatial connection between shelf and slope sand bands but they are separated by only 1 to 2 km. If there is some chute-directed down-slope transport of sand, perhaps it is/was more

active here but chute-directed slope-bypass of sand is not recognized as an important process compared to contour-directed transport.

6.4. Sand budget

In an attempt at establishing a sand budget for the winnowing hypothesis, estimates of erosion extent of the glacial muds and diamicts were calculated. The approach was to delineate areas of potential sand source up-slope of the individual sandwave fields and calculate erosion magnitude (thickness) necessary in order to balance with individual field sand volume estimates (Tables 1 and 2). These were based on assumed gravel and sand components of 5 and 25% respectively, typical for the parent glacial sediments. The sandwave formation process would have further sorted the sands, probably removing some of the fine sand. Thus, current sorting of the parent diamict would reduce to a residual amount, matching the sandwave sand grain size, of only about 10%. Assuming a collection (source) area limited to the uppermost slope and this 10:1 reduction requires vertical erosion of parent diamict between 50 and 150 cm for the northern fields (Table 2, second column from right). If the till area on the adjacent shelf is also added as potential winnowing source area, then winnowing thicknesses diminish to a 3 to 125 cm range (Table 2, right column) to balance with sand volume in the various fields. This invokes cross-shelf and down-slope sand transport distances of typically 5–10 km. The post-glacial eustatic lower-sea-level would have also acted to enhance shelf energy levels at that time. The greatest erosion estimate (125 cm) applies to

Table 1
Summary of sandwave field dimensions, height and wavelengths and symmetry derived from multibeam sonar bathymetric grid.

Field ID	Length km	Width km	Area sq. km	Water depth			No. measurements At 100 m spacing along crest	Height			Wavelength (crests)				Height wavelength ratio		Symmetry (positive is downstream; NW)			
				Maximum	Minimum	Mean		Maximum	Mean	SD	Maximum	Minimum	Mean	SD	H/W mean	SD	Maximum	Minimum	Mean	SD
N1	7	2.7	12	648	561	600	3840	2.5	0.4	0.3	205	15	58.6	23.8	0.019	0.011	14	−14	0.2	3.1
N2	20.1	1.8	26	564	645	606	4831	5.5	0.9	0.8	205	15	65.3	26.1	0.018	0.011	14	−14	0.6	3.0
N3	2.3	1	2	609	548	581	170	1.9	0.4	0.3	180	20	70.8	36.1	0.011	0.004	6	−12	−2.8	3.3
N4	4.1	1.4	6	623	550	588	567	2.2	0.5	0.4	200	15	71.0	34.9	0.010	0.004	14	−14	−1.1	4.5
N5	1.6	0.17	0	582	553	574	47	1.9	0.7	0.5	150	25	65.3	31.3	0.020	0.015	3	−13	−2.2	4.1
N6	2.2	0.4	1	702	652	671	0	Low amplitude and noisy data				−	−	−	−	−	−	−	−	−
S1	36	3.5	82	753	487	594	19182	5.5	0.8	0.6	205	15	55.8	22.0	0.020	0.015	17	−14	0.0	2.6
All fields	73	11	130	753	487	602	28637	5.5	0.6	0.5	205	15	64.5	29.0	0.016	0.010	17	−14	0.9	3.4

Table 2
Summary of sandwave slope metrics, backscatter and sand source and sink estimates.

Field ID	Slope, NW flank			Slope, SE flank			Slope ratio (negative suggests flow toward NW)				Backscatter strength, dB				Sandwave Field Volume Estimate (10 ⁶ m ³)	Winnowed source thickness estimate: sink volume equivalent at 10:1 reduction of parent diamict through winnowing				
	Maximum	Mean	SD	Maximum	Mean	SD	Minimum	Maximum	Mean	SD	Maximum	Minimum	Mean	SD		From morpho- metrics	Source area		Thickness equivalent	
																	Upslope source area only (km ²)	Upslope plus shelf source area (km ²)	Upslope winnowed thickness (cm)	Upslope and shelf winnowed thickness (cm)
N1	9.6	2.0	1.4	6.3	1.8	1.2	−14	16	0.4	2.6	−3	−35	−17.7	4.9	3.9	50.0	300.0	78	13	
N2	24.3	3.4	3.1	30.6	2.9	2.1	−31	48	0.2	3.8	−3	−39	−17.4	5.0	15.7	100.0	300.0	157	52	
N3	5.5	2.0	1.0	5.9	1.4	1.0	−9	19	1.7	3.6	−6	−37	−19.2	5.2	0.5	5.0	20.0	99	25	
N4	6.7	1.9	1.2	5.5	1.4	1.0	−14	16	0.9	4.0	−2	−36	−16.8	5.7	1.4	15.0	40.0	93	35	
N5	12.1	2.9	1.9	20.7	4.1	5.1	−12	7	0.1	4.1	−2	−32	−15.0	7.3	0.1	2.0	30.0	47	3	
N6	Low amplitude and noisy data						−	−	−	−	−	−	−	−	−	10.0	56.0	−	−	
S1	35.4	3.9	2.9	21.8	3.0	2.2	−54	77	0.7	3.7	2	−48	−17.8	6.2	50	170	400	295	125	
All fields	35.4	2.7	1.9	30.6	2.4	2.1	−54	77	0.6	3.6	2	−48	−17.3	5.7	72	352	1146	−	−	

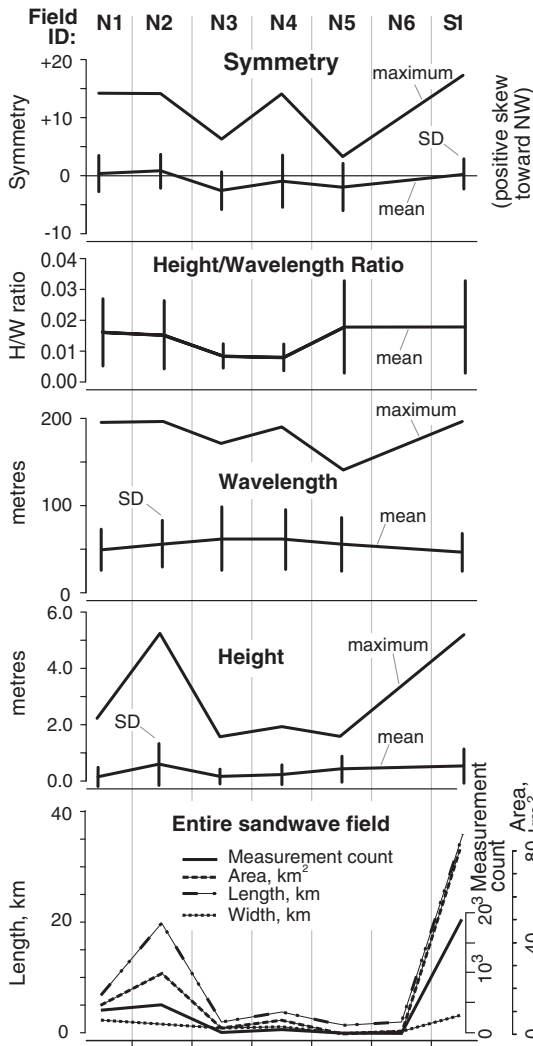


Fig. 14. Summary of basic bedform metrics for individual sandwave fields. Vertical lines are one sigma.

the large S1 field but this value would diminish if we were to invoke a greater and more far-travelled component of contouritic (not down-slope) sand source to this, the first (most upstream) in the string of

fields. This erosion amount is sufficient to produce observed thin, protective lags given gravel clast content in the nearby parent sediments of from one to eight percent (presumably higher in the till).

6.5. Sandwave field age

In the geologic setting section the observation was made that the sandwaves transect not only the GDF chutes but also the mass failure scarps cut in glaci-marine sediment overlying the debris flows. This places an early post-glacial maximum age on inception of the sandwaves. Slope-normal iceberg scours and long-transported ice rafted debris are early North Atlantic Drift indicators. The earliest inception would be when initial Atlantic water influx is recorded during the Bølling-Allerød interstadial (14.5 to 13.5 cal yr. B.P.) (Ślubowska-Woldengen et al., 2008), but they recognized stronger sub-surface inflow of saline water during the 9.5–7.5 cal yr. B.P. interval. If the sandwaves did not develop this early, then it probably was not until following the Neoglacial cooling (4.0–2.0 cal yr. B.P.) when fresh but sluggish circulation pertained (Ślubowska-Woldengen et al., 2008). An early inception does not necessarily require a closed sand budget at the time; what sand volume might have passed downslope has left no geologic record.

7. Discussion

The slope setting of the sandwave fields within the documented geostrophic contour current regime and the orientation of sandwave crests normal to the contours indicate a clear forcing of these sands by this geostrophic current. The CTD transect (Fig. 8) demonstrates the NAW and NSAIW water bodies and a spatial coincidence of the sandwave fields with the transition at the seabed. The transition depth between NAW and NSAIW has been observed to intersect the seabed between 600 and 400 m (Buhl-Mortensen et al., 2012; Ferré et al., 2012), connected to fluctuations in atmospheric forcing (Blindheim and Rey, 2004), but with small mean seasonal changes (Mork and Skagseth, 2010). Direct measurements at the site await analysis of results from recent current meter deployments. The spatial coincidence of the bedform fields with a significant water column thermo-halocline intersection of the seabed raises the question of which secondary oceanographic processes might influence the sandwaves.

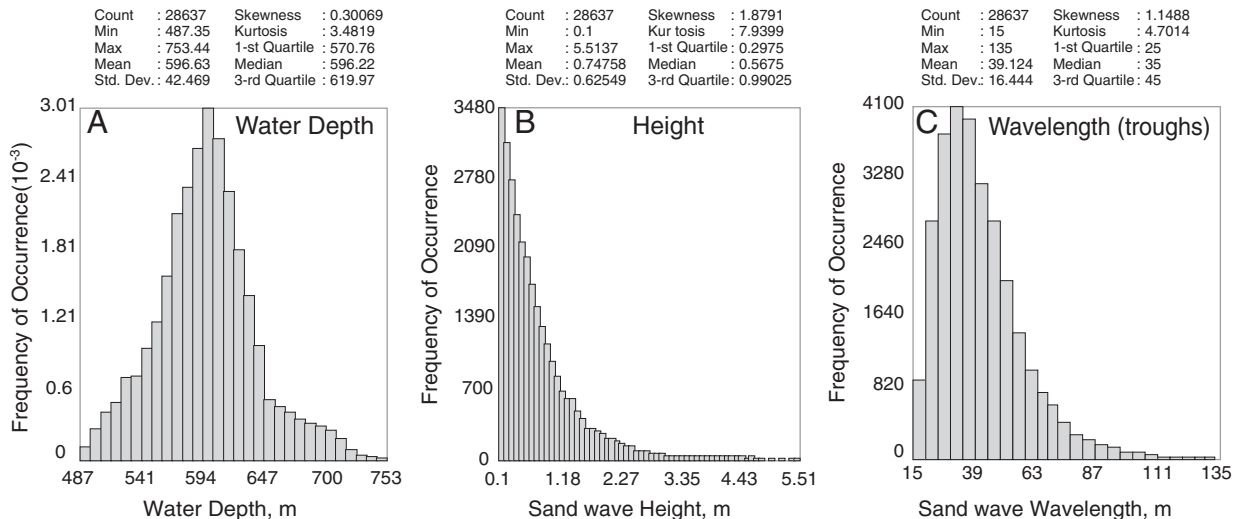


Fig. 15. Frequency distribution of sandwave water depths (a), heights (b) and wavelengths (c) for all fields.

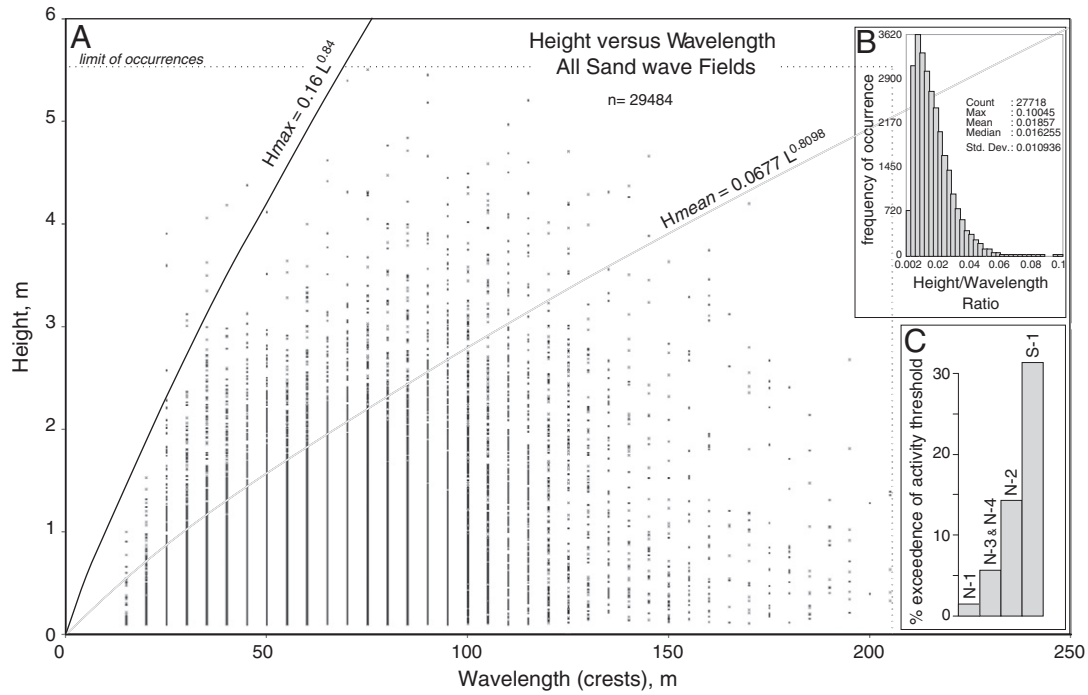


Fig. 16. Height versus wavelength plot (a) of all sandwaves in a context of activity level equations by Flemming (1980), H/L ratio frequency distribution (b), and comparison among fields of proportion of sandwaves deemed active by these criteria (c).

7.1. Sandwave activity

These bedforms are mid-range in size within a global context (Amos and King, 1984), the larger falling in the mid to large range. Generally, bedform size is positively related to current velocity (e.g. Rubin and McCulloch, 1980) and there is generally a grain size dependency, with coarser sands supporting higher forms. Accordingly, the larger sandwaves likely mark the core of the driving geostrophic stream and smaller flanking forms reflect diminishing current magnitude. However, there are several documented cases where bedform field boundaries are due to increased velocities, not decreased, where sand becomes

suspended instead of in traction, at least in fluvial/tidal examples. Other factors such as consolidation, lag deposits, and response time are also strong governors.

Small sandwaves tend to have a mean height/wavelength ratio of about 0.1 while that of active sandwaves is around 0.03, provided the sand source and development time is not limited (Dyer, 1986). Fig. 16b shows that examples above 0.03 are present but the bulk falls below this threshold. Flemming (1980) established another activity parameter based on height and wavelength and these equations are shown graphically in Fig. 16. Only about one quarter of the sandwave points fall above the H_{mean} curve denoting active forms. The largest

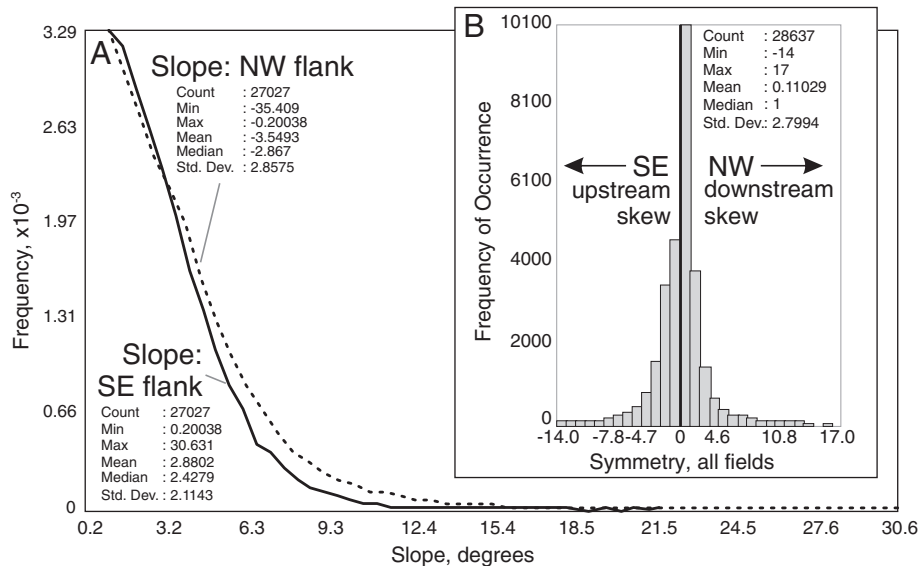


Fig. 17. Distribution of symmetry measurements for all fields (a). Comparison of the slope value distribution for NW (lee) and SE (stoss) flanks (b). The heavy black line (at value 0) marks symmetric forms. Distributions slightly favor a NW skew and a greater NW slope value, especially in the steeper (5 to 10°) range.

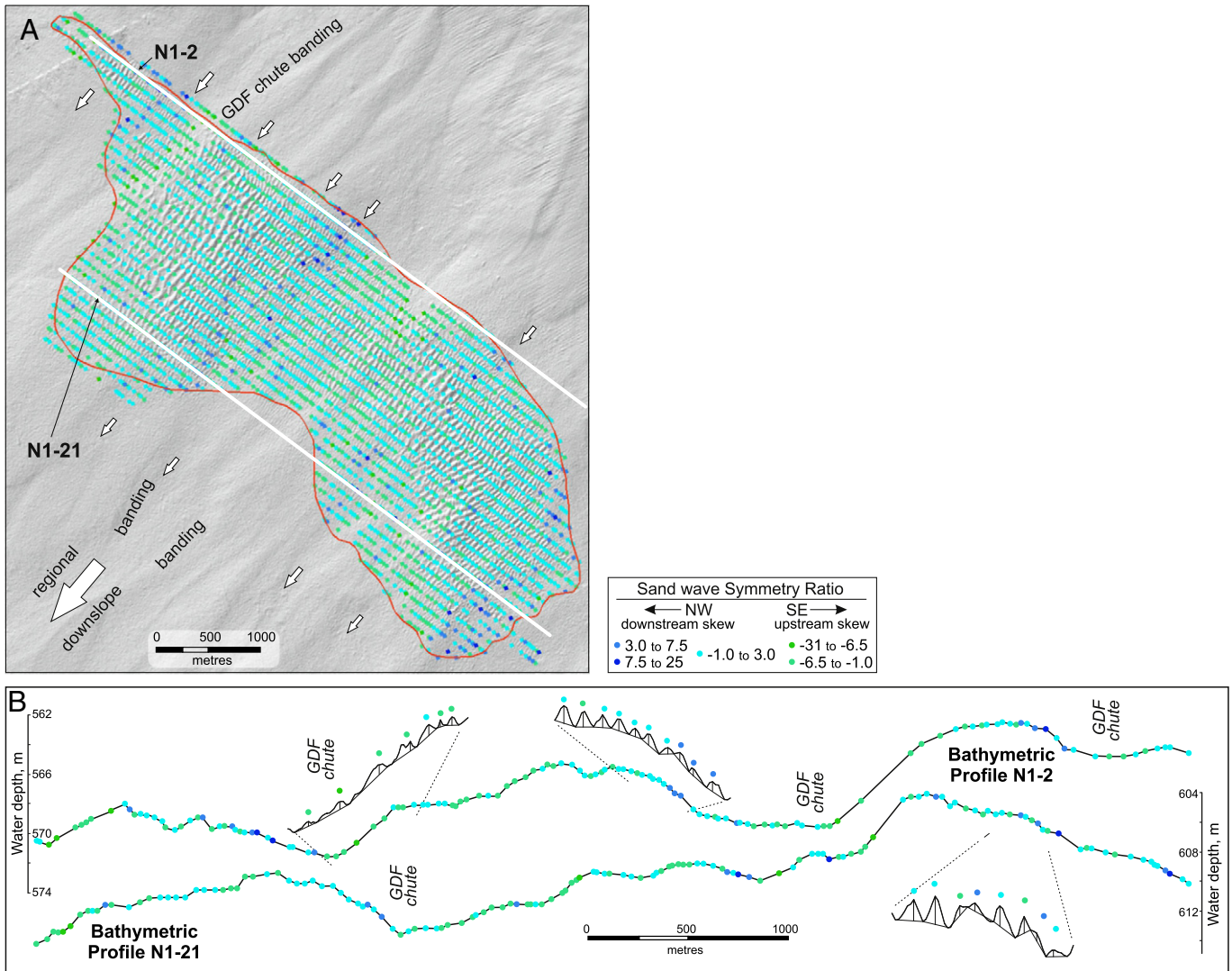


Fig. 18. Symmetry of bedforms in the N1 sandwave field superimposed on shaded relief bathymetry (a). Arrows demarcate thalwegs of GDF chutes. The color banding across the field follows the chutes. The sandwave symmetry is tuned to the GDF chute flanks (b) with an up-hill skew on opposite flanks, the NW flank examples apparently migrating against the main current.

fields, N2 and S1 contain proportionally many more active bedforms than other fields according to this criterion (Fig. 16c). Curiously, the smallest N3 and N4 fields appear more active than the N1, exceptions to a trend toward lower activity northward.

The video-observed ripples are clearly active, with sharp crests, asymmetries, and coarse troughs traction was observed during the 15 minute stationary portion of the R446 deployment. The stoss-situated 3-D forms generate from stronger currents than the lee-situated straight-crested examples. An active layer of centimeters to a decimeter is expected. The sharp cross-cutting of these two forms at the sandwave crest is too sharp to represent sandwave morphology-induced turbulence, directional spin or such reorganization of the currents. Rather it indicates non-synchronous, periodic changes in flow from sandwave crestline normal to crestline parallel. Lacking orientation of the video instrument restricts conclusions as to if this is up-slope or down-slope transport (or both).

Thus, the H-L metrics alone suggest that some bedforms are active while many are relatively moribund, with a greater proportion of active forms in the larger fields and a trend toward diminished activity to the north. Superimposed ripples indicate current activity but by more than one process; these are the mechanism by which the sandwaves are

mobilized. The steep sandwave lee slopes, not registered well from the sonar, further suggest a degree of activity.

7.2. Sand recycling

Inherent in a long-lived, closed but mobile sand system must be a mechanism for recycling most of the sand within each field. The near-normal distribution of sandwave profile symmetry and sandwave flanking slopes (Figs. 17 and 19) indicates mobility in both “upstream” and “downstream” directions and provides at least the potential for recycling of sand. In order to maintain the sand in a mid-slope setting, there must be an upslope component to the currents to counter the gravitational component. Fig. 20 shows a typical sandwave situation with superimposed gravity vectors. Here, the regional downslope dip magnitudes nearly match stoss-, and to a lesser degree lee-face slopes. The implication is that the gravitational component must be significant, acting on sand grains approximately normal to the geostrophic current. Cumulative downslope components with each grain movement would eventually remove sand out of the system (down the slope) were it not for a counteracting force. Though some leakage in a “closed” sand budget is likely, we have argued that sand source has diminished as protective lags developed. The implication is that much of the sand is

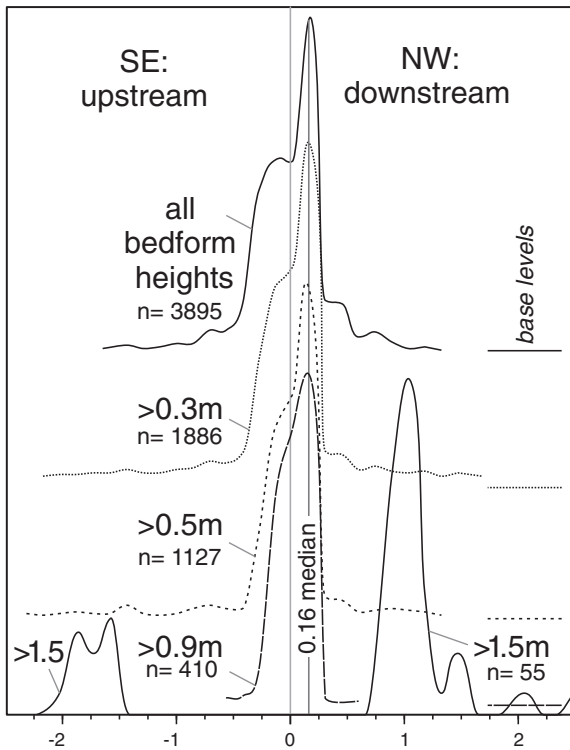


Fig. 19. Symmetry distributions of N1 field sandwaves for five height classes. Note the separation of base levels (zero occurrences) to minimize curve overlap.

recycled within the fields. The lee and trough-situated 2-D ripples are an obvious candidate for transfer of sand up (or down) the regional slope. If, contrary to our arguments, the sand budget is not closed and/or if

upstream and up-slope recycling is limited, this can only be reconciled with mobility of the sandwaves that is very slow but this contradicts most observations.

Establishing a sand budget potentially in balance only demonstrates that it is possible to generate and maintain the sands at this location on a long-term basis. It dictates a degree of sand mobility yet largely confined to field boundaries for long-term maintenance with a minimum flux of sand into and out of the field. Most observations are compatible with a dynamic system, more complex than simple feeding, bedform migration, and exiting of the sands from the fields. Of course, assumptions of sand source may be incorrect; present up-stream contour-current derived sand flux might be significant and sandwave migration proportionally active. Future work will address this.

7.3. Possible secondary oceanographic drivers: deep Ekman transport eddies and internal waves?

7.3.1. Long-term processes

Secondary processes inferred from the sandwave morphometrics are best related to relatively constant oceanographic processes with long term fluctuations or periodicities to which the inherently slow-responding large bedforms can tune. For instance, the meso-topographic-related domains in sandwave asymmetry (Figs. 18 and 19) representing components of current reversal, the requirement for long-term sand recycling, and the inferred up-slope sand transport component (from ripples) might be explained by the cumulative and/or combined effect of such processes, even if episodic. Potential influencing processes could be seasonal (winter) downwelling (as suggested in Rebesco et al., 2013), seasonal eddies, meandering of the isobath current, or deep Ekman rotation. Some elaboration follows.

Slope-situated topographic perturbations, such as the GDF chutes, would have similar cross-isobath effects on currents as those produced by small canyons, depending on their size. Modeling of canyon-effect in

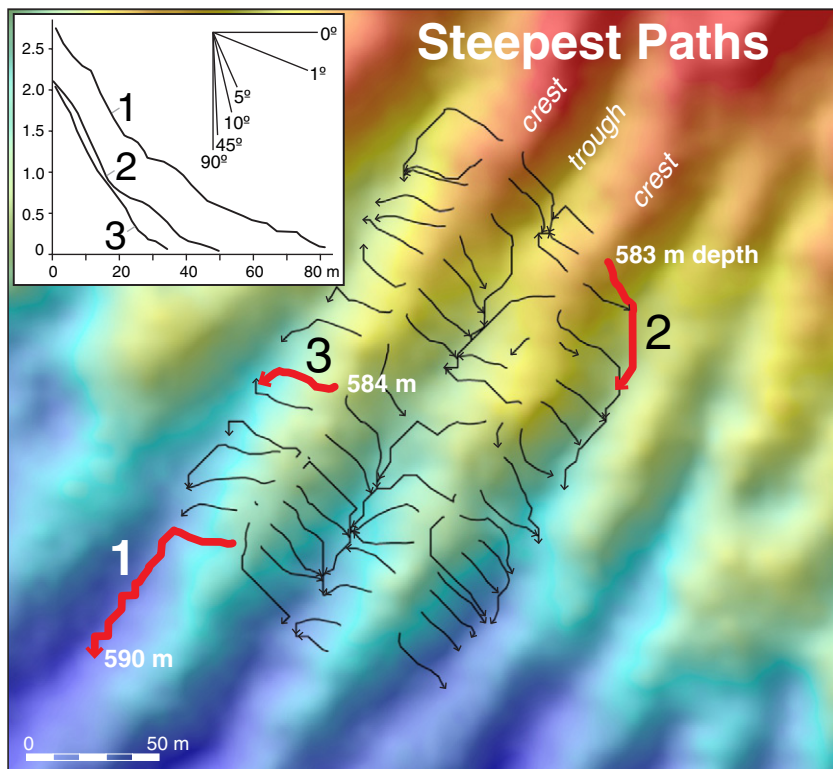


Fig. 20. Paths of maximum slope from selected crestline points. Three paths are highlighted with bathymetric profiles (insert). Most paths show an abrupt directional change at the base of the sandwave (trough), generally matching an inflection point in the corresponding profile. Below the inflection the regional slope is about 1°. A periodic up-slope sand transport is inferred to counter cumulative downslope drift and help maintain sand in the field.

some settings (e.g. Allen, 2004; Lima et al., 2007) can yield up- and down-welling and eddies so strong as to mask the isobath current. Geostrophic currents (as opposed to wind) can induce deep Ekman transport to the left (thus downslope, here) in the bottom boundary layer (e.g. Cushman-Roisin, 1994; Taylor and Sarkar, 2008). Heathershaw et al. (1998) inferred deep anti-cyclonic rotation through the Ekman effect from a mooring transect across the slope to the south, off Vestfjorden. This may explain down-slope migrating sand waves/ripples of vertical scales smaller than the bottom boundary layer thickness. Beyond this, temporal variability in both currents and vertical stratification of the water masses driven by different oceanographic mechanisms will influence the sandwaves in different seasons (e.g. Ramsden, 1995; Brink and Lentz, 2010). The combined vectors over long (seasonal?) timespans might, however, be sufficient to generate sandwave migration trends deviating from a simple northwesterly direction. The seabed effect of these may also migrate with long-term up- and down-slope movement of the stratified cold to warm transition.

7.3.2. Short-term processes

The strongest evidence for secondary current process is the very sharp crosscutting observation of the 2-D lee-face ripples on the stoss-situated 3-D ripples (Fig. 13); each set formed at a different time and at directions normal to the primary current. Any explanation needs only to invoke a short-term hydrologic process, as outlined below, given the short response time for ripples. A similar phenomenon, but on the shelf to the south had clear secondary tidal current influence (Bøe et al., 2009).

The effects of tide on sediment transport are not generally considered strong at great water depths but the cross-cutting ripple fields require a frequent, strong and temporally direction-changing driver. A slope to shelf mooring transect located to the south (off Vestfjorden, Heathershaw et al., 1998) demonstrated observations, consistent with models, indicating strong enhancements of K_2 and M_2 (diurnal and semi-diurnal) currents within the isobath current at depths similar to the Barents Sea sandwave fields. However, the magnitude of such secondary processes to the main geostrophic current at water depths over 700 m is not expected, acting on their own, to be sufficient for sand traction. Heathershaw et al. (1998) could not demonstrate internal tide-generated waves; neither have they yet been empirically demonstrated nor modeled in the area. However, the warm, mixed upper slope water and cool, less saline underlying water creates a potential interface for reflection of such waves to the seabed. This process can produce sufficient turbulent energy dissipation for sediment non-deposition, entrainment and erosion (e.g. Cacchione et al., 2002; Puig et al., 2004), including sandwave formation (Karl et al., 1986; Reeder et al., 2011). The Reeder et al. (2011) study suggests a strong influence for large sandwaves (up to 16 m amplitude) in the China Sea where exceptionally powerful tidally forced internal solitary waves impact the slope. The high frequency–short duration, high energy and potential for both up- and down-slope sediment mobility properties of internal waves are compatible with the interruption and overprinting of the geostrophic current as indicated by the cross-cutting ripple patterns. The studies cited here include end-member situations; the magnitude of these processes, if indeed they are extant for the Barents Sea examples, could be diminished in relation to the primary geostrophic current.

8. Summary and conclusions

Slope-situated, channelized GDFs derived from an ice sheet at the shelf break during the last glacial maximum and syn-depositional glacial marine muds with thin, winnowed, gravelly sand lag are locally overlain by thin sand bodies worked into sandwaves. Sandwave fields at between 500 and 700 m water depth range in width from 0.4 to 3.5 km and length from 1.6 to 36 km, totaling 130 km². Crestline orientations are consistently normal to the regional slope. These average 0.7 ± 0.6 m (maximum 5.5 m) height and 58 ± 24 m (maximum

205 m) wavelength, comprising fine to medium, well sorted sand. There is no stratigraphy or preservation of earlier sandwaves. The hemipelagic sediments failed locally as small rotational and translation slides but the sandwaves cross these, unaffected morphologically. Failures had to be post-glacial (after ca. 15 ka), broadly constraining sandwave field initiation. However, timing and magnitude of paleo-current evolution in early post-glacial times and, by proxy, the initiation and duration of sandwave activity are poorly constrained.

Volume considerations and lack of evidence for extensive down-slope sand transport from the Barents Sea shelf suggest that the sand source is local (within tens of km), derived from current winnowing of the uppermost glacial sediments distributed across the upper slope and outer shelf, leaving a lag on the muddy diamicts. A crude sand budget suggests a closed system whereby the sediment sink is largely within the sandwave bodies themselves.

A robust morphometric cataloguing of the bedforms allowed statistical presentations of several indices which suggest at least periodic mobility in at least sub-field domains of the bedforms. Height–wavelength ratios suggest up to 25% of the forms are active but insufficient sonar resolution tends to underestimate this. An active layer on the sandwaves demonstrated by current ripples includes starkly contrasting types and direction at the sharp sandwave crestline indicating a short-term up-and/or downwelling process. Tendency toward the expected net down-current (northwestward, contour-parallel) migration is demonstrated by bedform symmetry and stoss–lee slope differences but trends in the opposite direction nearly balance this. Long-term mobility of the larger bedforms must be inferred from their morphology until serial re-surveying is conducted.

There is an expression of local hydrologic steering in a tuning of bedform symmetry to the meso-morphology of the slope-parallel GDF chutes. Bedform asymmetries suggest up-hill migration on both “up-stream” and “downstream” flanks with respect to a northwestward flowing contour current. Furthermore, an upslope driving hydrologic component (normal to regional contours) is inferred to counter tendencies of gravity-driven grain migration.

A combination of inferred secondary currents, both arising from the stable or recurring eddies, and deep Ekman transport can contribute to both maintenance of sand within the fields on the mid-slope and to asymmetries through steering across GDF chute flanks. Tidal-driven internal waves along the transition between NSAIW and NAW, though not directly observed are a mechanism which could impact the slope at the sandwave field depth with sufficient energy and frequency to entrain sand in ripples. The spatial coincidence of the fields with the water mass interface, the seasonal migration of this zone across the full water depth range of the field, and an analogy with the demonstrated link between internal waves and slope-situated sandwaves in the China Sea all suggest an influence of these processes on the sandwave fields.

The relative impact of the oceanographic current and secondary processes remains to be answered through more detailed field study of the oceanography, sand stratigraphy and mid-term bedform mobility. Current measurements and high resolution numerical modeling experiments are planned to observe secondary oceanographic phenomena and to investigate topographic effects at the appropriate scale for explaining some of the sandwave morphological perturbations. Further, high resolution acoustic surveying to better map sand thickness, sampling for sedimentological analyses, and serial multibeam surveying to observe direct changes in sandwave patterns are planned.

Acknowledgments

The MAREANO program and the Norwegian Deepwater Programme (NDP) are thanked for data and financial support to publish this paper. The first author's participation in the project was under NGU auspices while on leave from the Geological Survey of Canada. The GSC

subsequently provided latitude for manuscript preparation in support of related goals on the Canadian margin. Benedicte Ferre is affiliated with the Centre of Excellence: Arctic Gas hydrate, Environment and Climate (CAGE) funded by the Norwegian Research Council (grant no. 223259). Michael Li, GSC-Atlantic, provided initial review. Jan Sverre Laberg, University of Tromsø and Adriano Viana, Petrobras kindly contributed to a better focus on the processes, manuscript clarity and attention to details with their reviews.

References

- Allen, J.R.L., 1980. Sand waves: a model of origin and internal structure. *Sedimentary Geology* 26, 281–328.
- Allen, S.E., 2004. Restrictions on deep flow across the shelf-break and the role of submarine canyons in facilitating such flow. *Surveys in Geophysics* 25, 221–247.
- Amos, C.L., King, E.L., 1984. Bedforms of the Canadian eastern seaboard: a comparison with global occurrences. *Marine Geology* 57, 167–208.
- Andreassen, K., Laberg, J.S., Vorren, T.O., 2008. Seafloor geomorphology of the SW Barents Sea and its glaci-dynamic implications. *Geomorphology* 97, 157–177.
- Ashley, G.M., 1990. Classification of large-scale subaqueous bedforms: a new look at an old problem. *Journal of Sedimentary Research* 60, 161–172.
- Baraza, J., Ercilla, G., Nelson, C.H., 1999. Potential geological hazards on the eastern Gulf of Cadiz slope (SW Spain). *Marine Geology* 155, 191–215.
- Belderson, R.H., Johnson, M.A., Kenyon, N.H., 1982. Bedforms. In: Stride, A.H. (Ed.), *Off-shore Tidal Sands: Processes and Deposits*. Chapman & Hall, London, pp. 27–57.
- Bellec, V.K., Wilson, M., Bøe, R., Rise, L., Thorsnes, T., Buhl-Mortensen, L., Buhl-Mortensen, P., 2008. Bottom currents interpreted from iceberg ploughmarks revealed by multibeam data at Tromsøflaket, Barents Sea. *Marine Geology* 249, 257–270.
- Bellec, V., Picard, K., Bøe, R., Thorsnes, T., Rise, L., Dolan, M., Elvenes, S., Lepland, A., Hansen, O.H., 2012a. Geologisk havbunnskart, Kart 71301600, September 2012. M 1: 100 000. Norges geologiske undersøkelse. <http://www.ngu.no/no/hm/Kart-og-data/Marinegeologiske-kart/havbunn-nedlasting/#Ferdige>.
- Bellec, V., Picard, K., Bøe, R., Thorsnes, T., Rise, L., Dolan, M., Elvenes, S., Lepland, A., Hansen, O.H., 2012b. Geologisk havbunnskart, Kart 71001600, September 2012. M 1: 100 000. Norges geologiske undersøkelse. <http://www.ngu.no/no/hm/Kart-og-data/Marinegeologiske-kart/havbunn-nedlasting/#Ferdige>.
- Blindheim, J., Rey, F., 2004. Water-mass formation and distributions in the Nordic Seas during the 1990s. *ICES Journal of Marine Science* 61, 846–863.
- Bøe, R., Bellec, V.K., Dolan, M.F.J., Buhl-Mortensen, P.B., Buhl-Mortensen, L., Rise, L., 2009. Giant sand waves in the Høla glacial trough off Vesterålen, North Norway. *Marine Geology* 267, 36–54.
- Bøe, R., Bellec, V., Thorsnes, T., Picard, K., Dolan, M., Rise, L., 2010. Tromsøflaket og Eggakanten. In: Buhl-Mortensen, L., Hodnesdal, H., Thorsnes, T. (Eds.), *Til bunns i Barentshavet og havområdene utenfor Lofoten - ny kunnskap fra MAREANO for økosystembasert forvaltning*. Norges Geologiske Undersøkelse, Trondheim, Norway, pp. 27–35 (128 pp. (English summary)).
- Brink, K.H., Lentz, S.J., 2010. Buoyancy arrest and bottom Ekman transport. Part II: oscillating flow. *Journal of Physical Oceanography* 40, 636–655.
- Buhl-Mortensen, P.B., Buhl-Mortensen, L., Dolan, M., Dannheim, J., Kröger, K., 2009. Mega-faunal diversity associated with marine landscapes of northern Norway: a preliminary assessment. *Norwegian Journal of Geology* 89, 163–171.
- Buhl-Mortensen, L., Hodnesdal, H., Thorsnes, T., 2010. Til bunns i Barentshavet og havområdene utenfor Lofoten - ny kunnskap fra MAREANO for økosystembasert forvaltning. *Norges Geologiske Undersøkelse, Trondheim, Norway* (128 pp. (English summary)).
- Buhl-Mortensen, L., Bøe, R., Dolan, M.F.J., Buhl-Mortensen, P.B., Thorsnes, T., Elvenes, S., Hodnesdal, H., 2012. 51 – banks, troughs, and canyons on the continental margin off Lofoten, Vesterålen, and Troms, Norway. In: Peter, T.H., Elaine, K.B. (Eds.), *Seafloor Geomorphology as Benthic Habitat*. Elsevier, London, pp. 703–715.
- Cacchione, D.A., Pratson, L.F., Ogston, A.S., 2002. The shaping of continental slopes by internal tides. *Science* 296, 724–727.
- Courtney, R., 2007. Storage and dissemination of SEG Y Data in JPEG2000 format. American Geophysical Union, Fall Meeting abstract #IN51B-0402.
- Cushman-Roisin, B., 1994. *Introduction to Geophysical Fluid Dynamics*. Englewood Cliffs, N.J., Prentice Hall.
- Damuth, J.E., 1980. Use of high-frequency (3.5–12 kHz) echograms in the study of near-bottom sedimentation processes in the deep-sea: a review. *Marine Geology* 38, 51–75.
- Dolan, M., Mortensen, P.B., Thorsnes, T., Buhl-Mortensen, L., Bellec, V.K., Bøe, R., 2009. Developing seabed nature-type maps offshore Norway: initial results from the MAREANO programme. *Norwegian Journal of Geology* 89, 17–28.
- Dyer, K.R., 1986. *Coastal and Estuarine Sediment Dynamics*. Wiley & Sons, Chichester, England.
- Ferré, B., Mienert, J., Feseker, T., 2012. Ocean temperature variability for the past 60 years on the Norwegian-Svalbard margin influences gas hydrate stability on human time scales. *Journal of Geophysical Research* 117 (C10017).
- Flemming, B.W., 1980. Sand transport and bedform patterns on the continental shelf between Durban and Port Elizabeth (southeast African continental margin). *Sedimentary Geology* 26, 179–205.
- Habgood, E.L., Kenyon, N.H., Masson, D.G., Akhmetzhanov, A., Weaver, P.P.E., Gardner, J., Mulder, T., 2003. Deep-water sediment wave fields, bottom current sand channels and gravity flow channel-lobe systems: Gulf of Cadiz, NE Atlantic. *Sedimentology* 50, 483–510.
- Hald, M., Vorren, T.O., 1984. Modern and Holocene foraminifera and sediments on the continental shelf off Troms, North Norway. *Boreas* 13, 133–154.
- Hanquiez, V., Mulder, T., Lecroart, P., Gonthier, E., Marchès, E., Voisset, M., 2007. High resolution seafloor images in the Gulf of Cadiz, Iberian margin. *Marine Geology* 246, 42–59.
- Hansen, B., Østerhus, S., 2000. North Atlantic-Nordic Seas exchanges. *Progress in Oceanography* 45 (2), 109–208.
- Haugan, P.M., Evensen, G., Johannessen, J.A., Johannessen, O.M., Pettersson, L.H., 1991. Modeled and observed mesoscale circulation and wave-current refraction during the 1988 Norwegian continental shelf experiment. *Journal of Geophysical Research* 96 (C6), 10487–10506.
- Heathershaw, A.D., Hall, P., Huthnance, J.M., 1998. Measurements of the slope current, tidal characteristics and variability west of Vestfjorden, Norway. *Continental Shelf Research* 18, 1419–1453.
- Heezen, B.C., Hollister, C.D., 1971. *The Face of the Deep*. Oxford University Press, New York.
- Helland-Hansen, B., Nansen, F., 1909. The Norwegian sea: its physical oceanography based upon Norwegian researches 1900–1904. Report on Norwegian Fishery and Marine investigations., vol. II 1909 Mo. 2. Det Mallingske bogtrykkeri, Kristiania (390 pp.).
- Hopkins, T.S., 1991. The GIN Sea – a synthesis of its physical oceanography and literature review 1972–1985. *Earth-Science Reviews* 30, 175–318.
- Karl, H.A., Cacchione, D.A., Carlson, P.R., 1986. Internal-wave currents as a mechanism to account for large sand waves in Navarinsky Canyon Head, Bering Sea. *Journal of Sedimentary Petrology* 56, 706–714.
- Kenyon, N.H., 1986. Evidence from bedforms for a strong poleward current along the upper continental slope of northwest Europe. *Marine Geology* 72, 186–198.
- Kenyon, N.H., Belderson, R.H., 1973. Bedforms of the Mediterranean undercurrent observed with sidescan sonar. *Sedimentary Geology* 9, 77–99.
- King, E.L., Sejrup, H.P., Haflidason, H., Elverhøi, A., Aarseth, I., 1996. Quaternary seismic stratigraphy of the North Sea Fan: glacially-fed gravity flow aprons, hemipelagic sediments, and large submarine slides. *Marine Geology* 130, 293–315.
- King, E.L., Bøe, R., Bellec, V.K., Rise, L., Dolan, M., 2011. Contour current driven sandwaves on the upper slope of the continental margin offshore northern Norway – setting and morphometrics. *NGU Report 2011.073* (93 pp.).
- Laberg, J.S., Vorren, T.O., 1993. A Late Pleistocene submarine slide on the Bear Island Trough Mouth Fan. *Geo-Marine Letters* 13, 227–234.
- Laberg, J.S., Vorren, T.O., 1995. Late Weichselian submarine debris flow deposits on the Bear Island Trough Mouth Fan. *Marine Geology* 127, 45–72.
- Laberg, J.S., Vorren, T.O., 2004. Weichselian and Holocene growth of the northern high-latitude Lofoten Contourite Drift on the continental slope of Norway. *Sedimentary Geology* 164, 1–17.
- Laberg, J.S., Vorren, T.O., Knutsen, S.M., 1999. The Lofoten contourite drift off Norway. *Marine Geology* 159, 1–6.
- Laberg, J.S., Andreassen, K., Knies, J., Vorren, T.O., Winsborrow, M., 2010. Late Pliocene–Pleistocene development of the Barents Sea ice sheet. *Geology* 38 (2), 107–110.
- Lima, J.A.M., Möller, O.O., Viana, A.R., Piovesan, R., 2007. Hydrodynamic modelling of bottom currents and sediment transport in the Canyon São Tomé (Brazil). In: Viana, A.R., Rebecco, M. (Eds.), *Geological Society, London, Special Publications*, 276, pp. 329–342.
- Masson, D.G., 2001. Sedimentary processes shaping the eastern slope of the Faeroe–Shetland Channel. *Continental Shelf Research* 21, 825–857.
- Michels, K.H., 2000. Inferring maximum geostrophic current velocities in the Norwegian–Greenland Sea from measurements of sediment surface samples: methods, application, and results. *Journal of Sedimentary Research* 70, 1036–1050.
- Mork, K.A., Skagseth, O., 2010. A quantitative description of the Norwegian Atlantic Current by combining altimetry and hydrography. *Ocean Science* 6 (4), 901–911.
- Mulder, T., 2003. Deep-water sediment wave fields, bottom current sand channels and gravity flow channel-lobe systems: Gulf of Cadiz, NE Atlantic. *Sedimentology* 50, 483–510.
- Nygård, A., Sejrup, H.P., Haflidason, H., King, E.L., 2002. Geometry and genesis of glacial debris flows on the North Sea Fan: TOBI imagery and deep-tow boomer evidence. *Marine Geology* 188, 15–33.
- Ottesen, D., Dowdeswell, J.A., Rise, L., 2005. Submarine landforms and the reconstruction of fast-flowing ice streams within a large Quaternary ice sheet: the 2,500 km-long Norwegian–Svalbard margin (57°–80° N). *Geological Society of America Bulletin* 117, 1033–1050.
- Poulain, P.-M., Warn-Varnas, A., Niiler, P.P., 1996. Near-surface circulation of the Nordic seas as measured by Lagrangian drifters. *Journal of Geophysical Research* 101, 237–258.
- Puig, P., Palanques, A., Guillén, J., El Khatib, M., 2004. Role of internal waves in the generation of nepheloid layers on the northwestern Alboran slope: implications for continental margin shaping. *Journal of Geophysical Research* 109 (C09011).
- Ramsden, D., 1995. Response of an oceanic bottom boundary-layer on a slope to interior flow. 1. Time-independent interior flow. *Journal of Physical Oceanography* 25, 1672–1687.
- Rebecco, M., Wählin, A., Laberg, J.S., Schauer, U., Beszczynska-Möller, A., Lucchi, R.G., Noormets, R., Accetella, D., Zarayskaya, Y., Diviacco, P., 2013. Quaternary contourite drifts of the Western Spitsbergen margin. *Deep-Sea Research Part I* 156–168.
- Reeder, D.B., Ma, B.B., Yang, Y.J., 2011. Very large subaqueous sand dunes on the upper continental slope in the South China Sea generated by episodic, shoaling deep-water internal solitary waves. *Marine Geology* 279, 12–18.
- Rubin, D.M., McCulloch, D.S., 1980. Single and superimposed bedforms: a synthesis of San Francisco Bay and flume observations. *Sedimentary Geology* 26, 207–231.
- Rudels, B., Friedrich, H.J., Quadfasel, D., 1999. The Arctic circumpolar boundary current. *Deep Sea Research Part II: Topical Studies in Oceanography* 46 (6–7), 1023–1062.

- Schlitzer, R., 2012. Ocean Data View. <http://odv.awi.de>.
- Ślubowska-Woldengen, M., Koç, N., Rasmussen, T.L., Klitgaard-Kristensen, D., Hald, M., Jennings, A.E., 2008. Time-slice reconstructions of ocean circulation changes on the continental shelf in the Nordic and Barents Seas during the last 16,000 cal yr BP. *Quaternary Science Reviews* 27, 1476–1492.
- Taylor, J.R., Sarkar, S., 2008. Stratification effects in a bottom Ekman layer. *Journal of Physical Oceanography* 38, 2535–2555.
- Viana, A.R., Faugères, J.-C., Stow, D.A.W., 1998a. Bottom-current-controlled sand deposits – a review of modern shallow- to deep-water environments. *Sedimentary Geology* 115, 53–80.
- Viana, A.R., Faugères, J.-C., Kowsmann, R.O., Lima, R.O., Caddah, J.A.M., Rizzo, J.G., 1998b. Hydrology, morphology and sedimentology of the Campos continental margin, offshore Brazil. In: Stow, D.A.W., Faugères, J.-C. (Eds.), *Contourites, Turbidites and Process Interaction*. *Sedimentary Geology*, 115, pp. 133–157.
- Vorren, T.O., Hald, M., Thomsen, E., 1984. Quaternary sediments and environments on the continental shelf off northern Norway. *Marine Geology* 57, 229–257.
- Vorren, T.O., Lebesbye, E., Andreassen, K., Larsen, K.-B., 1989. Glacigenic sediments on a passive continental margin as exemplified by the Barents Sea. *Marine Geology* 85, 251–272.
- Vorren, T.O., Laberg, J.S., Blaume, F., Dowdeswell, J.A., Kenyon, N.H., Mienert, J., Rumohr, J., Werner, F., 1998. The Norwegian–Greenland Sea continental margins: morphology and late Quaternary sedimentary processes and environment. *Quaternary Science Reviews* 17, 273–302.
- Winsborrow, M.C.M., Andreassen, K., Corner, G.D., Laberg, J.S., 2010. Deglaciation of a marine-based ice sheet: late Weichselian palaeo-ice dynamics and retreat in the southern Barents Sea reconstructed from onshore and offshore glacial geomorphology. *Quaternary Science Reviews* 29, 424–442.
- Wynn, R.B., Stow, D.A.V., 2002. Classification and characterisation of deep-water sediment waves. *Marine Geology* 192, 7–22.
- Wynn, R.B., Masson, D.G., Stow, D.A.V., Weaver, P.P.E., 2000. Turbidity current sediment waves on the submarine slopes of the western Canary Islands. *Marine Geology* 163, 185–198.